MOLYBDENUM SULFIDE PREPARED BY ATOMIC LAYER DEPOSITION: SYNTHESIS AND CHARACTERIZATION

by

Steven Payonk Letourneau

A dissertation

submitted in partial fulfillment

of the requirements for the degree of

Doctor of Philosophy in Materials Science and Engineering

Boise State University

May 2018

BOISE STATE UNIVERSITY GRADUATE COLLEGE

DEFENSE COMMITTEE AND FINAL READING APPROVALS

of the dissertation submitted by

Steven Payonk Letourneau

Dissertation Title: Molybdenum Sulfide Prepared by Atomic Layer Deposition: Synthesis and Characterization

Date of Final Oral Examination: 10 April 2018

The following individuals read and discussed the dissertation submitted by student Steven Payonk Letourneau, and they evaluated his presentation and response to questions during the final oral examination. They found that the student passed the final oral examination.

Elton Graugnard, Ph.D.	Chair, Supervisory Committee
Jeffrey W. Elam, Ph.D.	Member, Supervisory Committee
David Estrada, Ph.D.	Member, Supervisory Committee
Wan Kuang, Ph.D.	Member, Supervisory Committee
Dmitri Tenne, Ph.D.	Member, Supervisory Committee

The final reading approval of the dissertation was granted by Elton Graugnard, Ph.D., Chair of the Supervisory Committee. The dissertation was approved by the Graduate College.

ACKNOWLEDGMENTS

I first want to thank my family who has supported me through everything and never stopped believing in me. I need to thank my adviser who also supported me through all the trying times of my Ph.D. I also need to thank Dr. Jeffrey Elam and Dr. Anil Mane for all their help and generosity while at Argonne. Finally, I would like to thank all my colleagues at Boise State University and Argonne National Laboratory for their help and continued support through my Ph.D. I need especially to give thanks to all of my co-authors for their guidance and expertise.

I acknowledge support from the U.S. Department of Energy, Office of Science, Office of Workforce Development for Teachers and Scientists, Office of Science Graduate Student Research (SCGSR) program. The SCGSR program is administered by the Oak Ridge Institute for Science and Education for the DOE under Contract No. DE-SC0014664. This work made use of the XPS facility of the NUANCE Center at Northwestern University, which has received support from the Soft and Hybrid Nanotechnology Experimental (SHyNE) Resource (NSF NNCI-1542205). Use of the Center for Nanoscale Materials, including resources in the Electron Microscopy Center, was supported by the U.S. Department of Energy, Office of Science, Office of Basic Energy Sciences, under Contract No. DE-AC02-06CH11357. The work at Argonne was supported as part of the Center for Electrochemical Energy Science, an Energy Frontier Research Center funded by the U.S. Department of Energy (DOE), Office of Science, Office of Basic Energy Sciences. This research used resources of the Advanced Photon

Source, a U.S. Department of Energy (DOE) Office of Science User Facility operated for the DOE Office of Science by Argonne National Laboratory under Contract No. DE-AC02-06CH11357.

ABSTRACT

Molybdenum disulfide (MoS_2) is the prototypical two-dimensional (2D) semiconductor. Like graphite, it has a layered structure containing weak van der Waals bonding between layers, while exhibiting strong covalent bonding within layers. The weak secondary bonding allows for isolation of these 2D materials to single layers, like graphene. While bulk MoS_2 is an indirect band gap semiconductor with a band gap of ~1.3 eV, monolayer MoS_2 exhibits a direct band gap of ~1.8 eV, which is an attractive property for many opto-electronic applications. Atomic layer deposition (ALD) has been used to grow amorphous films of MoS_2 using molybdenum chlorides and carbonates, however many of these molybdenum chemistries require high temperature vapor transport as they are solids at room temperature. We demonstrate the first ALD of MoS_2 at 200 °C using molybdenum hexafluoride (MoF_6), a liquid at room temperature, and hydrogen sulfide (H_2S). *in situ* quartz crystal microbalance measurements were used to demonstrate self-limiting chemistry for both precursors, which is the hallmark of ALD. The deposited films were amorphous, and after annealing in hydrogen, crystalline MoS_2 was discernable. The nucleation and early stages of MoS_2 ALD on metal oxide surfaces were investigated using *in situ* Fourier transform infrared (FTIR) spectroscopy. The formation of Al-F and $MoOF_4$ seem to initially form, but after H_2S is introduced sulfate species begin to appear. This competition for oxygen seems to inhibit growth initially, until the oxygen at the surface is consumed and steady state growth occurs. To understand the structure of the amorphous films, X-ray absorption spectroscopy (XAS)

and high-energy X-ray diffraction (HE-XRD) experiments were performed at the Advanced Photon Source (APS) at Argonne National Laboratory (ANL). Contrary to previous findings, the MoS_2 structure was found to be sulfur rich; however, the atomic coordinations of Mo and S atoms bond distances matched standards. Interestingly, the Mo-Mo coordinations were much lower than reference structures, which could explain the lack of or very weak Raman vibrational modes seen in many as-deposited ALD MoS_2 films. Experimental data were consistent with films containing clusters of a sulfur rich $[Mo_3S(S_6)_2]^{2-}$ phase, but after annealing in H_2 and H_2S, these clusters decompose forming a layered MoS_2 structure. Understanding these complex surface interactions of nucleation, growth, and phase transformations is necessary to enable synthesis of high quality MoS_2 for use in future microelectronics.

TABLE OF CONTENTS

ACKNOWLEDGMENTS iv

ABSTRACT vi

LIST OF TABLES x

LIST OF FIGURES xi

LIST OF ABBREVIATIONS xv

CHAPTER ONE: INTRODUCTION 1

CHAPTER TWO: LITERATURE AND BACKGROUND 4

Atomic Layer Deposition 5

Molybdenum Disulfide 10

Molybdenum Hexafluoride, Hydrogen Sulfide, and Molybdenum Sulfide Growth 11

CHAPTER THREE: ATOMIC LAYER DEPOSITION OF MOS_2 USING MOF_6 AND H_2S 14

Atomic Layer Deposition of MoS_2 14

Experiment 16

Results and Discussion 18

Conclusions 29

CHAPTER FOUR: NUCLEATION OF MOS_2 ON ALUMINUM OXIDE 31

Experiment 32

Quartz Crystal Microbalance Experiments 32

in situ FTIR 33
Thin Film Growth and Characterization 34
Results and Discussion 35
Raman Spectroscopy Measurements 35
Quartz Crystal Microbalance Measurements 35
Fourier Transform Infrared Measurements 41
Film Characterization 48
Conclusions 52
CHAPTER FIVE: STRUCTURE OF ATOMIC LAYER DEPOSITED MoS_2 54
X-ray Absorption Spectroscopy and High Energy X-ray Diffraction 55
Experiment 57
Atomic Layer Deposition 57
Characterization 58
Results and Discussion 59
Conclusions 76
CHAPTER SIX: CONCLUSIONS 78
Summary 78
Outlook on 2D Materials in Electronics 79
REFERENCES 81

LIST OF TABLES

Table 1 Results adapted from the selectivity of MoF_6 on various surfaces reported by Lifshiz *et al.* [34]..... 12

Table 2 Summary of MoS_2 ALD. 14

Table 3 Data adapted from Li *et al.* showing the Raman fundamental peak positions as a function of the number of layers of exfoliated MoS_2 using 532 nm excitation[70]. 24

Table 4 Atomic percentages of the as-deposited and annealed films from XPS. .. 26

Table 5 Pulsing schemes for Al_2O_3 films grown on the ZrO_2 nanopowder and MoS_2 grown on the metal oxides for *in situ* FTIR measurements. ALD cycle pulses follow *Chemical A – Purge – Chemical B – Purge*..... 34

Table 6 Fitting parameters/results for Artemis structure fitting of MoS_2 films..... 66

Table 7 Fitting parameters and coordination numbers from RMC models of both amorphous and crystalline MoS_2 labeled *a* and *c* respectively. 72

LIST OF FIGURES

Fig. 1 Web of Science search results displayed from the year 2000 to 2017..... 2

Fig. 2 Schematic of a simple ALD system used for binary chemistries 6

Fig. 3 Illustration of an ALD cycle for a binary chemistry. A hydroxylated substrate is exposed to Chemical A (step 1). Once saturation is achieved, the chemical and by-products are purged out (step 2). Steric hindrance by the ligands can block neighboring sites that leads to a sub-angstrom growth per cycle. The second precursor, Chemical B, is dosed on the surface (step 3). Once this reaction completes, the excess chemical and by-products are purged out (step 4) yielding the final film with same surface chemistry that was started with. Repeating this ALD cycle controls film thickness..... 7

Fig. 4 Example schematic of an ALD window depending on the precursor type and its temperature dependence. 9

Fig. 5 Atomic simulations of the three primary allotropes of MoS_2. 2H stands for the hexagonal structure where each unit cell consists of 2 layers. 3-R is the rhombohedral structure where each unit cell consists of 3 layers, and finally 1-T which stands for the trigonal structure and only has a single layer in its unit cell..... 11

Fig. 6 QCM mass gains as a function of dose time, where the top plot is the variation with MoF_6 dose time while holding the H_2S dose time constant at 1 second. The bottom varies the H_2S does time while keeping the MoF_6 dose constant at 1.0 seconds. 19

Fig. 7 QCM measurements of MoS_2 where (a) is showing 15 ALD cycles and (b) is a single cycle of steady state MoS_2 growth..... 20

Fig. 8 (a) Spectroscopic ellipsometry measurements for various ALD cycle number with a linear fit line plotted on the data. (b) SEM image of 700 ALD cycle film annealed at 350 ℃. 23

Fig. 9 (a) Raman spectra of the as-deposited and annealed films using 514nm excitation where the as-deposited film lacks any Raman features, while the annealed films feature the in-plane and out-of-plane vibrational modes. (b) XRD scans of the as-deposited and annealed samples. A broad amorphous

peak and sharp substrate peak were observed around 32°. After annealing, the MoS_2 (002) peak is seen at 14°. 25

Fig. 10 High resolution scans of the (a) Mo3d region of the as-deposited, (b) Mo3d region of the annealed films, (c) S2p region of the as-deposited, and (d) S2p region of the annealed films. 26

Fig. 11 UV-vis measurements of MoS_2 on fused silica substrates. Samples were measured in a transmission geometry of various thickness (a). Fitting a line to the 12 nm samples, the optical band gap was determined in the Tauc plot. 29

Fig. 12 Raman spectra of 50 cycles of MoS_2 on ~20 nm of ALD Al_2O_3 at 150, 200, and 250 ℃. Dotted lines show where bulk modes should appear for layered MoS_2. The data have been offset for clarity. 35

Fig. 13 QCM measurments showing the measured mass changes for the first two cycles of MoS_2 on the Al_2O_3 coated crystal..... 37

Fig. 14 The mass change per complete AB cycle for each growth temperature is plotted for the first 24 cycles. The plots have been offset vertically with the steady state mass change indicated to the right of the axis. 40

Fig. 15 FTIR data of the first two cycles of MoS_2 deposited on ALD Al_2O_3 for 150, 200, and 250 ℃. Plots on top show the full range, where the OH stretches of the last water pulse (in red) can be seen above 3500 cm^{-1}. The lower plots show the lower frequencies where bulk modes of the metal atoms are present. The absorption scale was adjusted for each data set to maximize the peak heights and the y-axis scale varies between plots..... 42

Fig. 16 FTIR absorption measurements at (a) 150 ℃, (b) 200 ℃, and (c) 250 ℃. In each, the first two spectra, in red and black, are the last TMA and H_2O ALD half-cycles. Subsequent cycles numbers are labeled to the right of the axes. Dotted lines indicate key features: C-H bending mode at 1216 cm^{-1}, Mo=O stretch in MoF_4O at 1038 cm^{-1}, suspected Al-F species at 1002 cm^{-1}. 43

Fig. 17 Absorption spectra of MoS_2 deposited on ALD Al_2O_3 at 150, 200, and 250 ℃. Darker colors (starting with black) indicate early cycles, while red colors indicate the later cycles. 47

Fig. 18 A plot showing the baseline value for 10 cycles of MoS_2. The baseline was determined by the Y-intercept of a horizontal line fit to 1725 to 1675 cm^{-1} at each temperature. Each data point represents a single half-cycle of the AB chemistry. For consistency with the other plots, the first two data

points are from the last TMA and H_2O ALD half-cycles, while all others are alternation MoF_6 and H_2S. 48

Fig. 19 High resolution XPS scans of the Mo 3d and S 2p regions of 50 cycles of MoS_2 deposited on ~20 nm ALD Al_2O_3 at 150 ℃, 200 ℃, and 250 ℃. . 50

Fig. 20 Transmission electron micrscope images of cross-sections of as-deposited MoS_2 on ~ 20 nm of ALD Al_2O_3. The MoS_2 was deposited at (a) 200 ℃, and (b) 250 ℃. 52

Fig. 21 Illustration adapted from *The Fundamentals of XAFS* [104], showing the electron wave function of an ejected photoelectron perturbed by a neighboring atom. This scattering atom causes an energy change to the absorption energy that is displayed as "wiggles" in the absorption edge. Typically, the data is split into two regimes: the XANES region, which includes the absorption edge and near the edge features, and the EXAFS region, which contains longer order structure and can be fitted to known crystal structures. 56

Fig. 22 Raman spectra of as-deposited and annealed films. The as-deposited film lacks the characteristic Raman signals for layered MoS_2, but these signals appear after annealing for 30 min. at 400 ℃ and 600 ℃ in either H_2 or H_2S, indicating crystallization of the films. 60

Fig. 23 TEM images of 50 ALD cycles of MoS_2 on CNT-OH: (a) as-deposited, (b) following 400 ℃ 30 min anneal in H_2S, (c) following 600 ℃ 30 min anneal in H_2S. The as-deposited films appears amorphous, but a layered structure is observed for the annealed films. Approximatly 20 layers are formed on the CNTs after a 600 ℃ anneal in H_2S. 61

Fig. 24 X-ray absorption spectra of the Mo K edge for as-deposited MoS_2 on alumina powder and for annealed films. The spectrum of a MoS_2 reference powder is included for comparison. The data indicate similar Mo coordination environments for all films. 63

Fig. 25 XPS scans of the Mo 3d region of the (a) SiO_2 witness wafer and the CNT-OH nanotubes. (b) Is the fitted MoS_2 and MoO_x peaks with the S 2s region. 64

Fig. 26 Analyzed XAS data showing the (a) radial distribution of the scattering intensity around a Mo peak pair and (b) the reciprocal space scattering amplitudes. 65

Fig. 27 Coordination numbers of the Mo-S and Mo-Mo single scattering lengths for the as-deposted and annealed MoS_2 films, as well as a bulk MoS_2 reference. 67

Fig. 28 Normalized pair distributions from HE-XRD of MoS_2 deposited on CNT-OH comparing the as-deposited to annealed conditions in (a) H_2 and (b) H_2S. Zoomed in regions of the first few pair distances of (c) H_2 annealed and (d) H_2S anneal. Dotted lines are from a crystal file from of MoS_2 2H, which was simulated to determine where each contirbution of pair distances occur. Curves are offset vertically forclarity. 68

Fig. 29 High resolutions scan of S2p region showing two separate sulfur environments: S^{2-} and $S_{2.}$ 70

Fig. 30 Images of the starting models used as input structures for fullrmc for the (a) amorphous and (b) crystalline (2H phase) MoS_2 films. Both super cells fill a 50 $Å^3$ volume. Yellow spheres represent sulfur while the violet spheres are molybdenum..... 71

Fig. 31 (a) Shows a image of the simulated as-deposted film starting with an *amorphous* structure while (b) shows the 600 ℃ H_2S annealed model from a *crystalline* initial structure. (c) and (d) are the associated normalized pair distribution functions for the models forcomparions with the data. 73

Fig. 32 Bond pair analysis of the minimized structures from fullrmc. The bond length distribution of Mo-Mo (a), Mo-S (b), and S-S (c). For the as-deposited sample, the amorphous structure was used as the starting model, while the crystalline model was used for all of the annealed samples..... 76

LIST OF ABBREVIATIONS

ALD	Atomic Layer Deposition
CVD	Chemical Vapor Deposition
EXAFS	Extended X-ray Absorption Fine Structure
FTIR	Fourier Transform Infrared
FIBSEM	Focused Ion Beam Scanning Electron Microscope
FWHM	Full Width Half Max
GPC	Growth Per Cycle
ICSD	Inorganic Crystal Structure Database
PVD	Physical Vapor Deposition
MFC	Mass Flow Controller
MCPC	Mass Change Per Cycle
QCM	Quartz Crystal Microbalance
QMS	Quadrupole Mass Spectrometer
SEM	Scanning Electron Microscope
TEM	Transmission Electron Microscope
UHP	Ultra High Purity
XANES	X-ray Absorption Near Edge Structure
XAS	X-ray Absorption Spectroscopy
XPS	X-ray Photoelectron Spectroscopy
XRD	X-ray Diffraction

CHAPTER ONE: INTRODUCTION

As the end of Moore's law quickly approaches [1], new and advanced materials are needed to support the continued development of electronic devices for a wide array of applications, ranging from energy-efficient flexible electronics to light weight high capacity batteries. Two dimensional (2D) materials, which exploded into the scientific world following the mechanical exfoliation of graphite in 2004 to achieve single layer graphene [2], provide a new class of materials with novel properties well-suited to the next generation of electronic device technology [3], [4]. Soon after the discovery of graphene, the exfoliation technique was expanded to other layered materials, such as molybdenum disulfide (MoS_2), and niobium diselenide ($NbSe_2$) [5]. Graphene's dominance is clearly seen in Fig. 1 using Web of Science's topic search, using the general search terms: "graphene", "molybdenum disulfide OR MoS_2", and "atomic layer deposition OR ALD". In 2017 there were a staggering 28,818 matches, while the MoS_2 and ALD record hits barely reached one quarter of this value when combined.

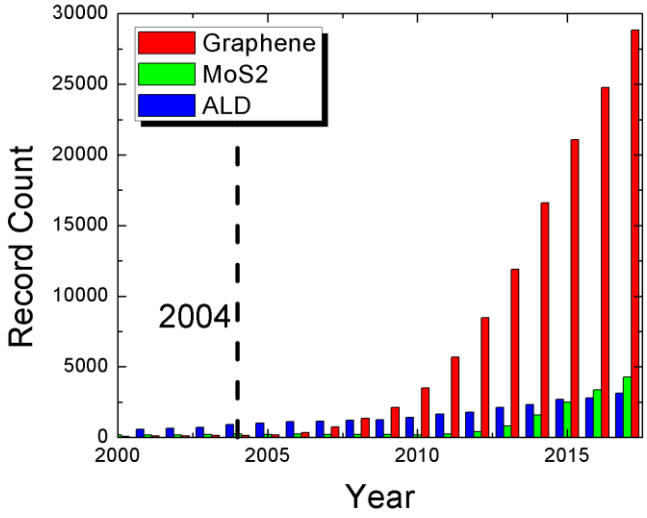

Fig. 1 Web of Science search results displayed from the year 2000 to 2017.

One drawback to graphene for many device applications is that it is not a natural semiconductor and therefore does not have a band gap. Although inducing a band gap is possible, this makes it a non-ideal candidate to replace silicon in transistors [6], [7]. While graphene consists of a single layer of carbon atoms, a single layer of MoS_2 consists of a layer of molybdenum atoms sandwiched between two layers of sulfur atoms. For many 2D semiconductors, the band gap of the material is dependent on the number of layers present. In its bulk form (>5 layers) MoS_2 exhibits an indirect band gap of 1.3 eV, while a single layer has a direct band gap of 1.8 eV [8]. This specific property and carrier mobilities reported as high as 192 $cm^2V^{-1}s^{-1}$ [9], has driven much of the research in developing new techniques to integrate the growth of monolayer MoS_2 into current semiconductor processes. Currently, much of the high quality MoS_2 results from mechanically exfoliated materials and high temperature chemical growth processes. Neither of these processes are compatible with high-volume semiconductor device manufacturing. Atomic layer deposition (ALD) has become a crucial step in any

microelectronic device fabrication. To date, very little research has been put into the ALD of MoS_2 and with only a handful of chemistries reported (see Table 2 for full list).

In this dissertation, the growth of MoS_2 by ALD using molybdenum hexafluoride (MoF_6) and hydrogen sulfide (H_2S) is demonstrated and the films are characterized. Self-limiting chemistry was observed for both precursors and a growth mechanism was proposed based on *in situ* measurements. The nucleation of the films on aluminum oxide was probed to understand how MoF_6 and H_2S interacts on dielectric substrates. Using X-ray absorption spectroscopy (XAS), the structure of as-deposited films was characterized. Understanding the interfacial reactions is crucial for MoS_2 in electronic applications.

CHAPTER TWO: LITERATURE AND BACKGROUND

The deposition of thin films has a long history, however much of the advancement in film deposition technologies did not occur until high quality vacuum systems were invented [10]. Vacuum deposition started with physical vapor deposition (PVD) processes stemming from the evaporation of noble metal wire [10]. Chemical vapor deposition (CVD) is relatively old, first referenced in 1880 by Powell, Oxley and Blocher using CVD to coat the filaments of incandescent lamps with carbon or metal to improve their strength [11]. It was not until the 1960s that CVD, as is it typically known today, was used in traditional microelectronics [12]. CVD is typically a fast growth process where one or more non-reacting chemicals are introduced into a vacuum chamber in the vapor phase. The sample or substrate is heated, driving the free energy of reaction negative, so a chemical reaction occurs, ideally, only on the surface of the heated sample. Controlling the growth relies primarily on the partial pressures of the two chemicals above the surface of the material and temperature [12].

CVD growth rates have been reported to range from to 10,000 to 250,000 Å per minute [13]. However, the process is limited to non-reacting chemicals as they are mixed in the gas phase and rely on a heat source to promote film growth [14]. Difficulty can arise when trying to coat high surface area features or deep structures [15]. This issue will only become more difficult as the geometries of structures continue to decrease [16]. Atomic layer deposition (ALD) is able to fill this gap in the deposition world, exhibiting excellent thickness control and the ability to produced conformal films, even on very high

surface area substrates [17]. Importantly, ALD can utilize chemical precursors that are more reactive than those used in CVD, and this allows the deposition temperature to be lower for ALD than CVD.

Atomic Layer Deposition

Atomic layer deposition (ALD) in the traditional sense was developed by Dr. Tuomo Suntola in the 1970s to coat thin films on electroluminescent flat panel displays [18]. At the time, the process was referred to as Atomic Layer Epitaxy (ALE), which soon was changed, as many materials did not grow in an epitaxial method. Although Suntola is given much of the credit to the developing the technique, the first published work mentioning a "self-limiting" method came out of Russia by Professor V. B. Aleskovskii and his student S. I. Kol'tsov, referred to as molecular layering technique (ML) [19].

ALD is a chemical vapor deposition process where the chemical precursors are introduced sequentially into a vacuum chamber. ALD systems can vary greatly, depending on their purpose and scale. A typical system consists of a reaction chamber, vacuum pump, mass flow controller (MFC), computer-controlled dosing valves, and a manifold for chemical delivery, as illustrated in Fig. 2. A MFC is typically used to control the flow of inert carrier gas past the dosing valves and into the chamber. Many of the precursors used in ALD have a low vapor pressure and this carrier gas aids in the vapor transport of the chemical. When a dose valve is opened the chemical diffuses into the manifold and carried to the reaction chamber by the carrier gas. The amount of precursor is controlled by the time the dose valve is opened, however even after the dose valve is closed, chemical may still be diffusing through the system. Characterizing the

precursor dose can be done by measuring the system's pressure or with *in situ* tools, like a quadrupole mass spectrometers (QMS). Carrier gas is continuously flowed through the system and once a dose is complete, it will purge any remaining precursor or by-products. ALD growth is temperature dependent, meaning sample temperature must be well-controlled. This is done externally, either as in an isothermal system where the entire chamber is heated, or by a local heater in the chamber, which is known as a cold-walled reactor. In either system, an ALD cycle is controlled by sequentially dosing the chemicals into the reaction chamber.

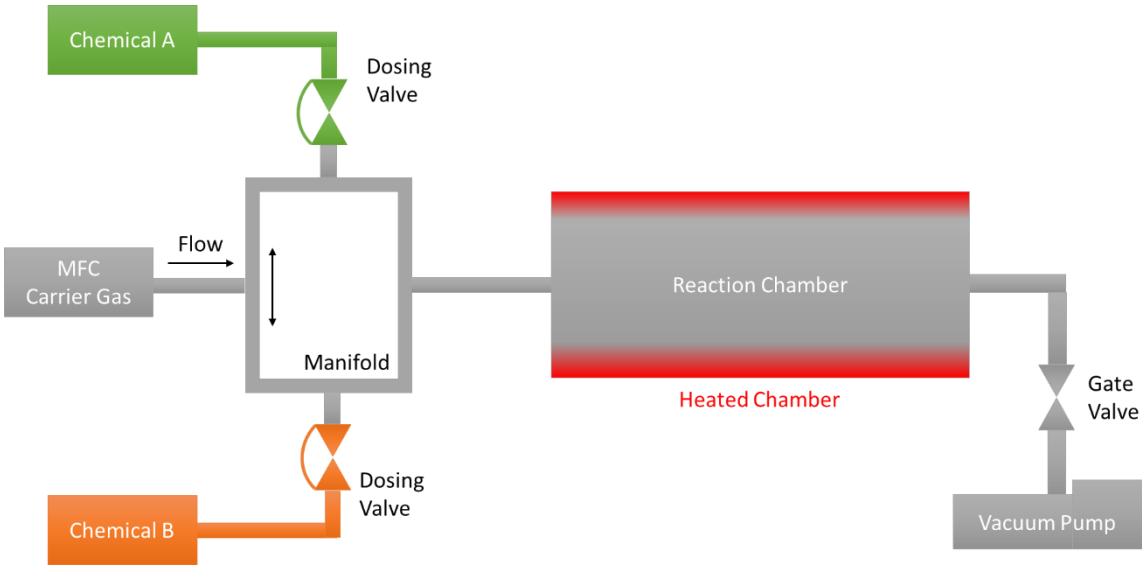

Fig. 2 Schematic of a simple ALD system used for binary chemistries

Because the chemicals are introduced sequentially, they can be highly reactive with each other. One of the hallmarks of ALD is "self-limiting" growth behavior, where the precursor reacts with all available reaction surface sites at which point the reactions stop since the precursors are chosen to be thermally stable and not self-reactive. Unlike in traditional CVD, where a constant flow of precursors is introduced above the samples,

ALD is broken up into what is known as ALD cycles. For binary chemistries, this consists of four parts, as illustrated in Fig. 3.

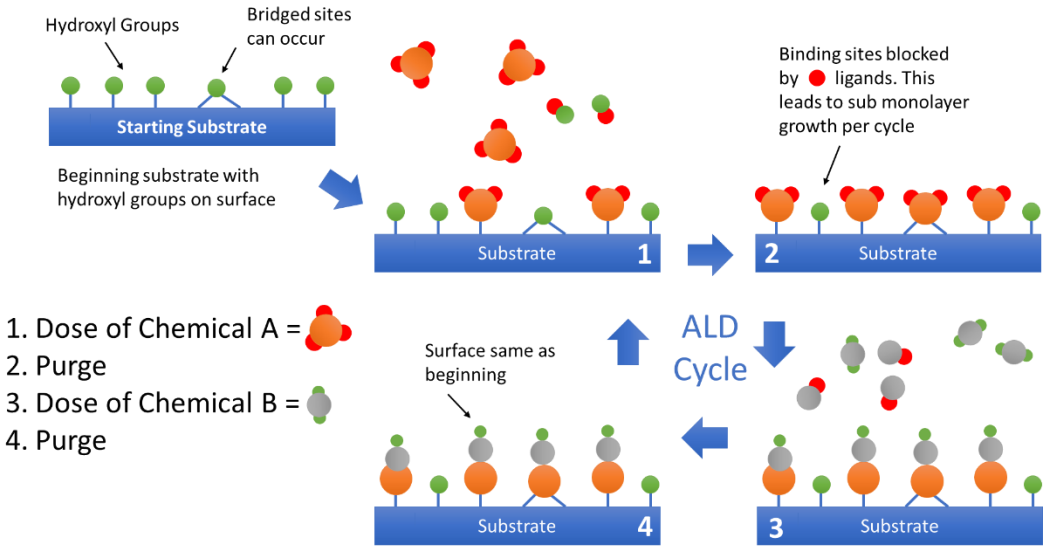

Fig. 3 Illustration of an ALD cycle for a binary chemistry. A hydroxylated substrate is exposed to Chemical A (step 1). Once saturation is achieved, the chemical and by-products are purged out (step 2). Steric hindrance by the ligands can block neighboring sites that leads to a sub-angstrom growth per cycle. The second precursor, Chemical B, is dosed on the surface (step 3). Once this reaction completes, the excess chemical and by-products are purged out (step 4) yielding the final film with same surface chemistry that was started with. Repeating this ALD cycle controls film thickness.

The first step consists of dosing the first precursor (Chemical A) in the reactor chamber, which chemisorbs on the surface. This is followed by a purge step, where the dosing valve is closed and the by-products and excess chemical are removed by the constant flow of carrier gas. The third step is where second precursor (Chemical B) is dosed into the reactor chamber, finishing the surface reaction and preparing the surface chemistry for the next ALD cycle. The last step is another purge, where any excess precursor and by-products are removed. This cyclical growth behavior allows for very precise thickness control which is typically sub-monolayer per cycle [17]. The formation of the film, from a binary chemistry, can be ideally formulated as:

$$A(g) + B(g) \rightarrow Flim\ (s) + Byproducts(g) \qquad \text{Eq. 1}$$

where (g) denotes a gaseous species and (s) denotes solid. This reaction can be further broken down into two "half-reactions". These half-reactions outline the surface reactions that occur on the substrate during steps one and three outlined in Fig. 3. It becomes useful to use a real system to explain this and the prototypical ALD chemistry is the growth of aluminum oxide using trimethylaluminum (TMA) and water (H_2O). Eq. 2 shows the overall reaction for growing a film of Al_2O_3 from two molecules of TMA. The first half-reaction, Eq. 3, starts with a surface of hydroxyl terminated aluminum atoms, where the "*" denotes the surface species. During the dosing of TMA, a single methyl group will react with the surface and form methane as a by-product. This leaves a chemisorbed aluminum species on the surface with two remaining methyl groups. The stoichiometry in Eq. 3 is idealized, where experiments has shown on average approximately 1.5 ligands leave the TMA during this chemisorption step [20]. Eq. 4 shows the final reaction, the dose of the water, where the left-over methyl groups react, again forming methane as a by-product and leaving a hydroxyl bound to the aluminum. Notably, the reaction ends with the same surface species with which it started. This prepares the surface for the next ALD cycle.

$$2Al(CH_3)_3(g) + 3H_2O(g) \rightarrow Al_2O_3(s) + 6CH_4(g) \qquad \text{Eq. 2}$$

$$AlOH^* + Al(CH_3)_3 \rightarrow AlOAl(CH_3)_2^* + CH_4 \qquad \text{Eq. 3}$$

$$AlCH_3^* + H_2O \rightarrow AlOH^* + CH_4 \qquad \text{Eq. 4}$$

As previously mentioned, the growth per cycle is typically less than one monolayer of material because the ligands of the metal ion can block neighboring binding sites. Thus, for many materials, the growth per cycle (GPC) is very low, and the TMA and H_2O chemistry yields a GPC of 1.1 Å per cycle [20].

The self-limiting nature of ALD is temperature dependent and is characterized by what is called an ALD window [17]. While some chemistries lack an ALD window [21], this can help understand non-ideal ALD behavior. In the ALD window, shown in Fig. 4, growth is self-limiting and the thickness of the film per cycle does not change over a particular temperature range. Below the window, condensation of the precursor will increase the growth, while a mass loss can occur because of a chemical's lower reactivity at reduced temperatures. Above the ALD window, the chemicals can start to decompose and deposit in a CVD type growth. On the other hand, if the reacted precursors or reaction sites become volatile, a decrease can be observed as they leave the surface.

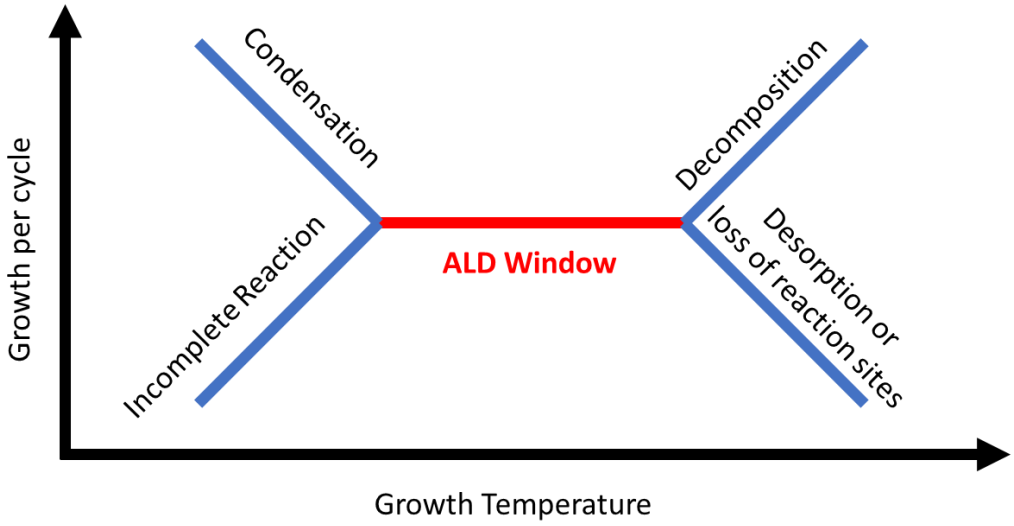

Fig. 4 Example schematic of an ALD window depending on the precursor type and its temperature dependence.

Molybdenum Disulfide

Molybdenum disulfide (MoS_2) is a layered material analogous to graphite. It is a naturally occurring material which can be found in molybdenum mines in Colorado and China [22]. The material has been used unknowingly as a lubricant for centuries as its properties and appearance made it indistinguishable to graphite [22]. Patents as early as 1927 outlined its use as a dry lubricant [23]. MoS_2 exhibits two primary bonding types: weak van der Waals bonds between layers and covalent bonding with-in the layer between the molybdenum and sulfur atoms [24]. It can be found in three different phases: 2H, 3-R, and 1-T, as shown in Fig. 5. Each designation refers to the space group and the number of layers present in a single unit cell. The hexagonal (2H) and rhombohedral (3-R) structures are the most stable and naturally occurring phases. The 1-T structure is unique in that it is meta-stable and instead of semiconducting, it is metallic in nature [25], [26]. The 1-T structure can be visualized in orthogonal coordinates in an orthorhombic unit cell, however authors have reported it in a tetragonal cell which is incorrect [27]–[30]. The T in the phase stands for *trigonal,* which at some point got lost in translation [31]. The trigonal cell is outlined in Fig. 5.

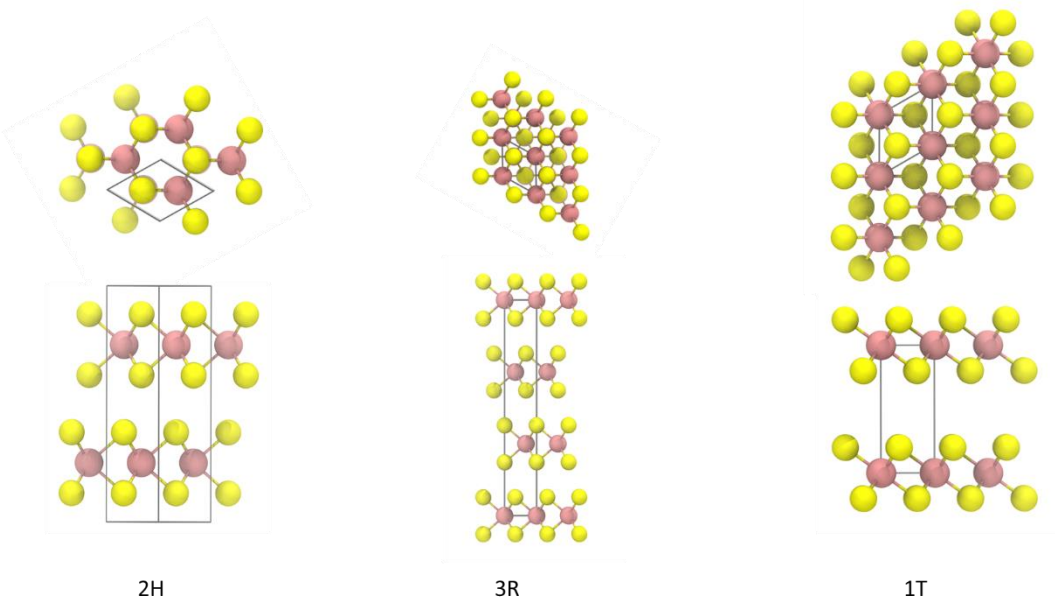

Fig. 5 Atomic simulations of the three primary allotropes of MoS_2. 2H stands for the hexagonal structure where each unit cell consists of 2 layers. 3-R is the rhombohedral structure where each unit cell consists of 3 layers, and finally 1-T which stands for the trigonal structure and only has a single layer in its unit cell

Molybdenum Hexafluoride, Hydrogen Sulfide, and Molybdenum Sulfide Growth

Reports from 1931 measured the vapor pressure and thermodynamic properties of MoF_6 [32], however much of the current property data is from Osbourne *et al.* [33]. MoF_6 is a liquid at room temperature, which has a high vapor pressure of approximately 400 Torr and is a gas above 35 ℃ [33]. This makes it one of the few liquid molybdenum precursors available.

Lifshiz *et al.* used low pressure chemical vapor deposition (LPCVD) to grow molybdenum metal at 200-400 ℃ in H_2 and found a magnitude difference in growth rate between 200 and 250 ℃ at the same flow rate [34]. An interesting finding was the selective behavior of the precursor on various surfaces. Table 1 is adapted from this work to summarize the findings:

Table 1 Results adapted from the selectivity of MoF_6 on various surfaces reported by Lifshiz *et al.* [34]

Substrate	Result
LPCVD W	Consumes W, deposits Mo after Si surface is exposed
Sputtered Al	Does not deposit on Al, forms a thin layer of AlF_3
Sputtered TiN	Consumes TiN, deposits once Si is exposed
Sputtered Co	Formed an unknown film, maybe $CoSi_2$
$CoSi_2$	Deposits Mo on top by consuming Si
Sputtered $TaSi_2$	Does not deposit on $TaSi_2$, roughens surface
Sputtered PtSi	Slowly consumed PtSi

As selective ALD gains more attention, these results may play a role in future use of this precursor. Lee *et al.* reported a thermodynamic study of the possible reaction products of the Mo-S-F-H system using calculations and found that excess H_2S is typically required to yield MoS_2 [35]. The following year, using CVD, Lee showed that the growth orientation of the basal planes was temperature dependent; below 320 ℃ films grew with the basal plane parallel to a SiO_2 substrate, but grew perpendicular above 420 ℃ [36]. In the same year, 1995, Orij *et al.* summarized much of the CVD work with MoF_6, and modeled the growth of MoF_6 on SiO_2, finding it to not be self-limiting [37]. Two reports from Sahin *et al.* [38], [39], contrary to Orij, found self-limiting growth, which Orij explained because of a very low partial pressure above the heated sample stage in the cold wall reactor used in Sahin's setup [37]. Using thermogravimetric measurements, Gama *et al.* showed that molybdenum disilicide reacted with HF and F_2 to form MoF_6 and SiH_4 readily [40]. Seghete *et al.* demonstrated the very first use of MoF_6 in ALD, with the deposition of molybdenum metal using disilane as the co-reactant [41]. Seghete found self-limiting behavior, confirmed by quartz crystal microbalance (QCM) measurements, at a temperature range of 90 - 150 ℃. High growth rates were found for the Mo, which was attributed to the MoF_6 reacting with itself [41].

From these reports, much of the research using molybdenum hexafluoride has involved CVD of Mo metal and MoS_2. The reactivity of MoF_6 and silicon, and the lack of self-limiting ALD are major hurdles to overcome when attempting to incorporate the chemistry into silicon-based electronics. However, similar chemistries, like WF_6, have been used to deposit metal in via contacts [42] and the reported surface chemistry selectivity has the possibility to reduce fabrication steps [43]. Moreover, the report of ALD of Mo demonstrates this chemistry acts in a self-limiting behavior when the reactants are separated, as is done in ALD. This makes the MoF_6 and H_2S chemistry an excellent candidate for use in the ALD of MoS_2.

CHAPTER THREE: ATOMIC LAYER DEPOSITION OF MOS_2 USING MOF_6 AND H_2S

Atomic Layer Deposition of MoS_2

ALD of MoS_2 has first demonstrated by Tan *et al.* in 2014 using $MoCl_5$ and H_2S on c-sapphire [44]. Monolayer and few layer MoS_2 growths were achieved and confirmed by atomic force microscopy (AFM) and transmission electron microscope (TEM) measurements. The as-deposited films were amorphous in nature and to obtain high quality films, a high temperature anneal in sulfur was needed. Table 2 outlines the current literature and chemistries used in the ALD of MoS_2.

Table 2 Summary of MoS_2 ALD.

Chemistry A	Chemistry B	Layered as-deposited	Anneal	Ref
$MoCl_5$	H_2S	N	Y	[44], [45]
$MoCl_5$	H_2S	Y	N	[46]–[49]
$MoCl_5$	H_2S plasma	Y	N	[50], [51]
$MoCl_5$	$(CH_3)_2S_2$	Y	N	[52]
$Mo(CO)_6$	H_2S	N	N	[53]
$Mo(CO)_6$	H_2S	N	Y	[54]
$Mo(CO)_6$	H_2S	Y	Y	[55]
$Mo(CO)_6$	H_2S plasma	Y	Y	[56]
$Mo(CO)_6$	$(CH_3)_2S_2$	N	Y	[57]–[59]
$Mo(CO)_6$	$(CH_3)_2S_2$	N	N	[60]
$Mo(CO)_6$	$(CH_3)_2(CH_2)_2S/(CH_3)_2S_2$	Y	N	[61]
$Mo(CO)_6$	$((CH_3)Si)_2S$	N	Y	[58]
$Mo(NMe_2)_4$	H_2S	N	Y	[62]
$Mo(NMe_2)_4$	$(CH_3)_2S_2$	N	Y	[63]
$Mo(thd)_3$	H_2S	Y	N	[64]
MoF_6	H_2S	N	Y	[65]*,[66]*

* author's work

The most popular chemistry for MoS_2 ALD is $MoCl_5$ and H_2S. This is analogous to $TiCl_4$ and H_2O, where the by-products of the reaction are TiO_2 and HCl gas [67]. ALD MoS_2 has lower mobilities than exfoliated or CVD grown films due to the significantly higher disorder and defect densities of ALD films. This demands newer processes and a better understanding of the factors that produce defects.

In this work, we demonstrate MoS_2 ALD using MoF_6 and H_2S. Since MoF_6 is a high vapor pressure liquid at room temperature, it has a practical advantage over other Mo precursors as it does not need to be heated or sublimed for delivery [33]. MoF_6 has previously been used as an ALD precursor to deposit Mo metal on various surfaces using disilane as the co-reactant [41]. They found MoF_6 was self-limiting but could react with itself on the surface, which explained the larger than expected growth rates. MoF_6 has two primary routes for reduction:

$$2MoF_6(g) + 3Si(s) \rightarrow 2Mo(s) + 3SiF_4(g), \quad \text{Eq. 5}$$

$$MoF_6(g) + 3H_2(g) \rightarrow Mo(s) + 6HF(g). \quad \text{Eq. 6}$$

The free energy of reaction (ΔG) is -891 kJ/mol for Eq. 5 and -50 kJ/mol for Eq. 6 [68]. The co-reactant, H_2S, is a gas at room temperature and is commonly used as a sulfurizing agent, as seen in Table 2. Similar to earlier reports of MoF_6, self-limiting behavior through *in situ* QCM measurements at 200 ℃ was observed, which is indicative of ALD growth. The as-deposited films were found to be X-ray amorphous, which is typical for ALD films, and lack a layered structure. However, after annealing at 350 ℃ in H_2, crystalline peaks were observed corresponding to the interplanar layers of MoS_2. The optical band gap matched bulk values, of 1.3 eV, after annealing [8].

Experiment

For all of the experiments in this work, the ALD growth was performed in a custom built, viscous flow, hot walled reactors that has been discussed previously [69]. For this experiment, the reactor was kept at 200 ℃ with a base pressure of approximately 1 Torr. Valve control, pressure, and QCM measurements were synchronized through LabVIEW software. MoF_6 and H_2S precursors have high vapor pressures at room temperature and extremely dangerous. Special precautions are needed due to the flammability/toxicity of H_2S and the corrosive nature of MoF_6. Vented cabinets with fire suppression contained multiple cross-purge assemblies that allowed for safely handling bottle exchanges and leak testing. The ALD timing sequences are expressed as t_1 - t_2 - t_3 - t_4 where t_1 and t_3 are the MoF_6 and H_2S dose times, respectively, and t_2 and t_4 are the corresponding purge times, and all times are in seconds.

MoF_6 (Sigma Aldrich 98%) and H_2S (99.5% Matheson Trigas) were dosed using typical ALD cycles as described above. Some of the samples were placed onto a hot stage and inserted into the ALD reactor. The samples were held in place by a fine mesh allowing the reduction gas to reach the surface of the samples. To increase the partial pressure of the reducing gas, the system's base pressure was increased by reducing the conductance to the pump. Ultra high purity (UHP) hydrogen was dosed continuously into the reactor while the temperature was increased to 350 ℃ and held for 15 minutes. H_2 was flowed continuously until the sample cooled down to approximately 200 ℃ (the deposition temperature).

A modified Maxtek QCM sensor head with a RC cut crystal was used for *in situ* measurements of the mass changes. To prevent deposition on the back side of the crystal,

the crystal was adhered to the head with silver paste and carrier gas was flowed through the sensor head [69]. Using a needle valve, the flow of the backside purge was adjusted so the process pressure increased by 5 %. Prior to measurements, the system was kept at a constant temperature for 6 to 8 hours so that the QCM sensor reached thermal equilibrium.

X-ray photoelectron spectroscopy (XPS) measurements were carried out at the KECKII/NUANCE facility at Northwestern University on a Thermo Scientific ESCALAB 250 Xi (Al Ka radiation, hν = 1486.6 eV) equipped with an electron flood gun. Lower resolution survey scans and high-resolution scans of the Mo and S 3d, 2s and 2p electron energies were performed. The XPS data were analyzed using Thermo Avantage software and all spectra were referenced to the C1s peak (284.8 eV). Peak deconvolution in the high-resolution spectra (Mo 3d, S 2p) was performed using the Powell fitting algorithm with 30% mixed Gaussian–Lorentzian fitted peaks in all cases. Fitting procedures were based on constraining the spin-orbit split doublet peak areas and full-width half-maximum (FWHM) according to the relevant core level.

Raman spectroscopy (inVia, Renishaw) was used to probe the layered structure. The E_{2g} and A_{1g} vibrational modes arise from the in-plane and out-of-plane modes, respectively [70]. Backscattering measurements were performed using an excitation wavelength of 514.5 nm of a 12mW Ar^+ laser on all samples. A 50x objective produced a spot size of ~1 μm. To prevent sample damage, a neutral density filter of 5% – 10% transmission was used.

A Bruker D2 Phaser X-ray diffractometer (XRD) using a Cu Kα source in Bragg-Brentano geometry was used to probe the crystallinity and crystal structure of the MoS_2.

A J. A. Woollam, Inc. α-SE Ellipsometer (Lincoln, NE) was used to measure the thickness of the films using a Cauchy model.

Results and Discussion

Thermodynamic calculations of the Gibbs free energy (ΔG) using HSC Chemistry were performed on two possible growth routes for MoS_2: *direct* and *in-direct* [71]. For the direct route the reaction of MoF_6 and H_2S would yield MoS_2, HF gas, and elemental sulfur (Eq. 7) yielding a free energy of -379 kJ/mol. The in-direct method involves the formation of MoS_3 (Eq. 8) followed by a subsequent annealing step (Eq. 9) in hydrogen to obtain MoS_2. The free energy of formation of MoS_3 is -409 kJ/mol and the annealing step is -24 kJ/mol. It's interesting to note that the free energy of formation of MoS_3 is lower than that of MoS_2.

$$MoF_6(\mathrm{g}) + 3H_2S(g) \rightarrow MoS_2(\mathrm{s}) + 6HF(g) + S(s) \quad \text{Eq. 7}$$

$$MoF_6(\mathrm{g}) + 3H_2S(g) \rightarrow MoS_3(\mathrm{S}) + 6HF(g) \quad \text{Eq. 8}$$

$$MoS_3(\mathrm{s}) + H_2(\mathrm{g}) \rightarrow MoS_2(\mathrm{s}) + H_2S(g) \quad \text{Eq. 9}$$

One explanation for the lower reaction energy of MoS_3 could be that this route does not need to reduce molybdenum from Mo^{6+} to Mo^{4+}.

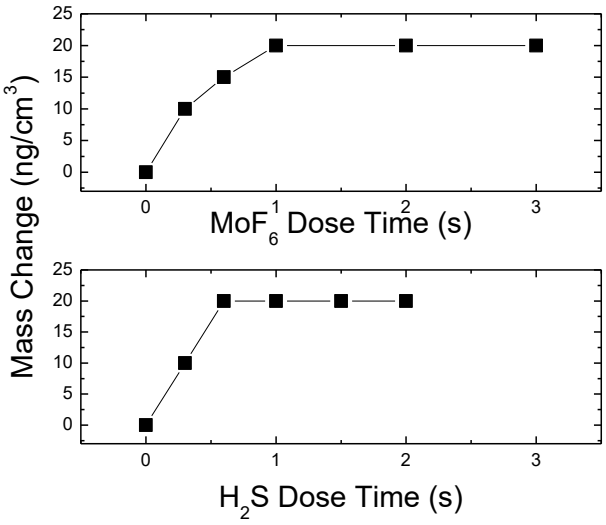

Fig. 6 QCM mass gains as a function of dose time, where the top plot is the variation with MoF_6 dose time while holding the H_2S dose time constant at 1 second. The bottom varies the H_2S does time while keeping the MoF_6 dose constant at 1.0 seconds.

Mass gain measurements by QCM in Fig. 6 demonstrate self-limiting behavior as a function of dose timing for both precursors. From these QCM studies, a dosing scheme of 1.5-15-1.5-15was used. Linear growth is observed over many cycles in Fig. 7(a), over approximately 15 cycles. A growth per cycle (GPC) of approximately 0.4 Å was calculated using the crystalline density of MoS_2 of 5 g/cm^3. A single cycle is shown in Fig. 7(b), with the mass changes between each half-cycle labeled. A long desorption slope is observed after the MoF_6 pulse, ending with a mass gain of 23 ng/cm^2. After the H_2S pulse the mass decreases by 6 ng/cm^2 yielding a net mass gain of 17 ng/cm^2.

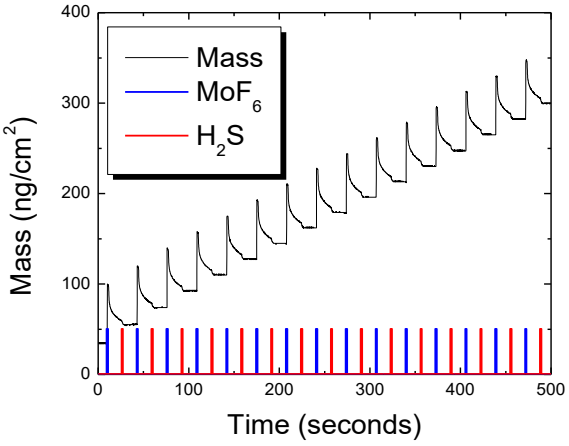

(a)

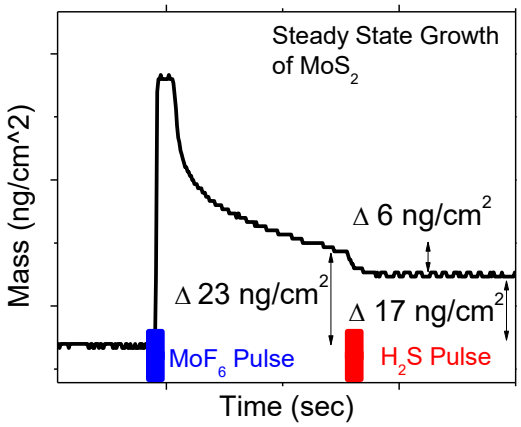

(b)

Fig. 7 QCM measurements of MoS_2 where (a) is showing 15 ALD cycles and (b) is a single cycle of steady state MoS_2 growth.

Using the relative mass changes, we evaluate which growth mechanism (direct vs. indirect) is the most probable. Assuming the direct method occurs through thiol exchange (Eq. 7), we can propose the following surface reactions:

$$(SH)_x^* + MoF_6(g) \rightarrow (S)_x MoF_{(6-x)}^* + xHF(g), \quad \text{Eq. 10}$$

$$(S)_x MoF_{(6-x)}^* + 3H_2S(g) \rightarrow S_2Mo(SH)_x^* + S(s)^* + (6-x)HF(g), \quad \text{Eq. 11}$$

where surface species are designated with a "*". In Eq. 10, MoF_6 reacts with *x* surface thiol (SH) groups liberating *x*HF molecules leaving (6-*x*) F atoms remain bound to the Mo. In the second half reaction, Eq. 11, the new surface reacts with H_2S and releases the remaining (6-*x*) F atoms. In the process, HF vapor and solid S are produced, yielding a newly formed MoS_2 species that is terminated with xSH groups so the original surface functionality is restored. We hypothesize that the sulfur sublimes as S_8(g) which is a reasonable assumption since sulfur has a vapor pressure of ~2 Torr at 200 ℃ [72]. We can define a mass ratio for this direct method as:

$$R = {}^{\Delta m_a}/_{\Delta m} = {}^{(210-20x)}/_{160}, \qquad \text{Eq. 12}$$

where Δm_a is the mass change from Eq. 10 and Δm is the mass change for a complete cycle. Knowing the molecular weights, the average step from the QCM data in Fig. 7(b) gives an R of 1.32(± 0.05). Assuming, $x = 0$ in Eq. 12, meaning that no thiols are involved with the ALD process, an R value is calculated to be 1.31, agreeing closely with the measurement.

Alternatively, if we assume the growth mechanism follows the indirect route the half reactions are:

$$(SH)_x^* + MoF_6(g) \rightarrow (S)_x MoF_{(6-x)}^* + xHF(g), \qquad \text{Eq. 13}$$
$$(S)_x MoF_{(6-x)}^* + 3H_2S(g) \rightarrow S_3Mo(SH)_x^* + S(s) + (6-x)HF(g). \qquad \text{Eq. 14}$$

The reactions in Eq. 10 and Eq. 13 are identical as the first half-reaction does not differ between the two routes. The difference arises in the second half-reaction where the product contains an extra S (Eq. 14). We can again calculate the mass change ratio for the equations:

$$R = {\Delta m_a}/{\Delta m} = {(210 - 20x)}/{192} \quad \text{Eq. 15}$$

For this reaction when x = 0, R = 1.09 and when x = 6, R = 0.47. Comparing this to the experimental QCM step ratio of R=1.32, the data imply that the direct method is the probable method as the experimental mass ratio is greater than any value of *x* for the indirect method. The slow mass loss during the MoF_6 purge time could be the slow sublimation of sulfur from the surface as a result from previous pulses.

Samples were grown on (001) silicon with a native oxide and fused silicon substrates. Using spectroscopic ellipsometry, the thickness of 100, 300, 600, and 1000 ALD cycle samples grown at 200 ℃ were measured. Fig. 8(a) shows a near linear growth rate. However, the thickness of the 100 ℃ samples was measured to be 60 Å and 750 Å for the 1000 cycle samples, which corresponds to a GPC of 0.6 and 0.75 Å/cycle, respectively. This is higher than our original measurement of 0.46 Å/cycle, which was determined from 19 ALD cycles of QCM data. An explanation for this is that the morphology of the sample is not continuous, as seen in Fig. 8(b). A platelet type growth was found for the 700 cycle sample, where the platelets were around 20-30 nm in size. This platelet formation will effectively increase the surface area resulting in a larger growth per cycles. We believe that these higher growths per cycle values were not observed by QCM because we did not record data beyond a few hundred cycles. It must be noted that thickness measurements measured by ellipsometry becomes more difficult to interpret. However, we assume that the film is growing between the platelets and the underlying film is increasing in thickness.

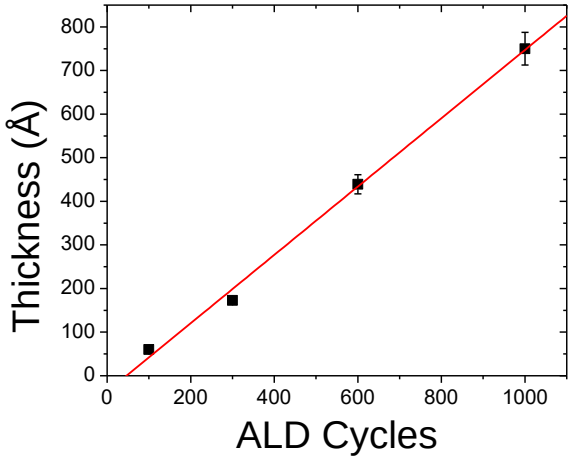

(a)

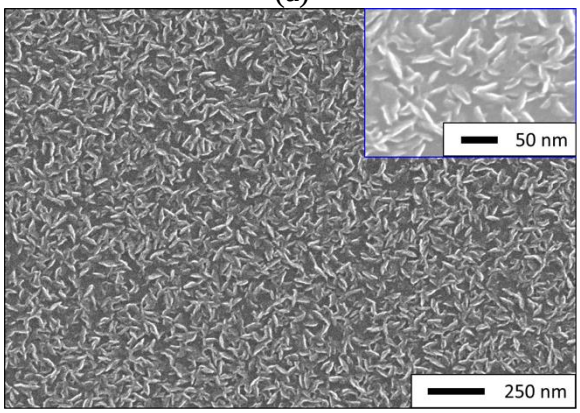

(b)

Fig. 8 (a) Spectroscopic ellipsometry measurements for various ALD cycle number with a linear fit line plotted on the data. (b) SEM image of 700 ALD cycle film annealed at 350 °C.

Raman spectroscopy is one of the most common techniques used to characterize 2D materials. MoS_2 has been well characterized and has two primary modes: E_{2g}^1 and A_{1g}, which correspond to the in-plane and out-of-plane vibrational modes, respectively. The separation between these modes has been used for determining the number of layers using multiple excitation wavelengths [70]. Table 3 shows the typical values found for mechanically exfoliated MoS_2 and the differences using an excitation wavelength of 532 nm.

Table 3 Data adapted from Li *et al.* showing the Raman fundamental peak positions as a function of the number of layers of exfoliated MoS_2 using 532 nm excitation[70].

Thickness	E^1_{2g} (cm^{-1})	A_{1g} (cm^{-1})	Difference (cm^{-1})
1 Layer	384.7	402.7	18.0
2 Layer	382.5	404.9	22.4
3 Layer	382.4	405.7	23.3
4 Layer	382.4	406.7	24.3
Bulk	383.0	407.8	24.8

Interestingly, as seen in Fig. 9(a), Raman measurements of the as-deposited ALD MoS_2 did not show any Raman peaks. After annealing, the characteristic Raman peaks for MoS_2 could be seen, as-well as a (002) reflection in the XRD spectrum in Fig. 9(b). The E^1_{2g} and A_{1g} peaks were observed at ~380 cm^{-1} and ~409 cm^{-1}, respectively. These differ from the tabulated data in Table 3 and these shifts are attributed to disorder in the films. The peak position of 14 ° was consistent with the reported layer spacing for the MoS_2 2H phase [73].

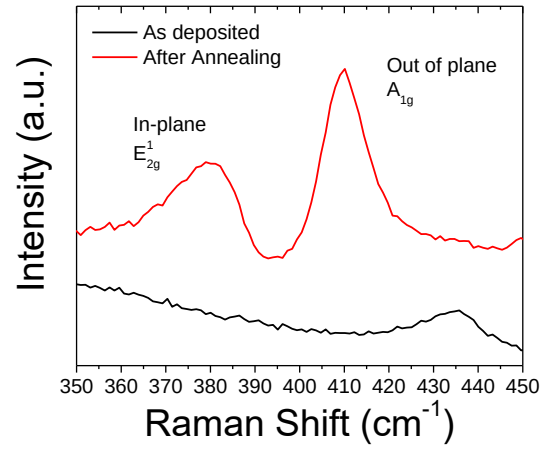

(a)

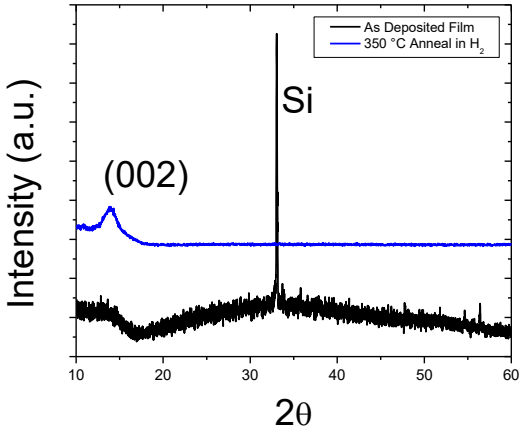

(b)

Fig. 9 (a) Raman spectra of the as-deposited and annealed films using 514nm excitation where the as-deposited film lacks any Raman features, while the annealed films feature the in-plane and out-of-plane vibrational modes. (b) XRD scans of the as-deposited and annealed samples. A broad amorphous peak and sharp substrate peak were observed around 32°. After annealing, the MoS_2 (002) peak is seen at 14°.

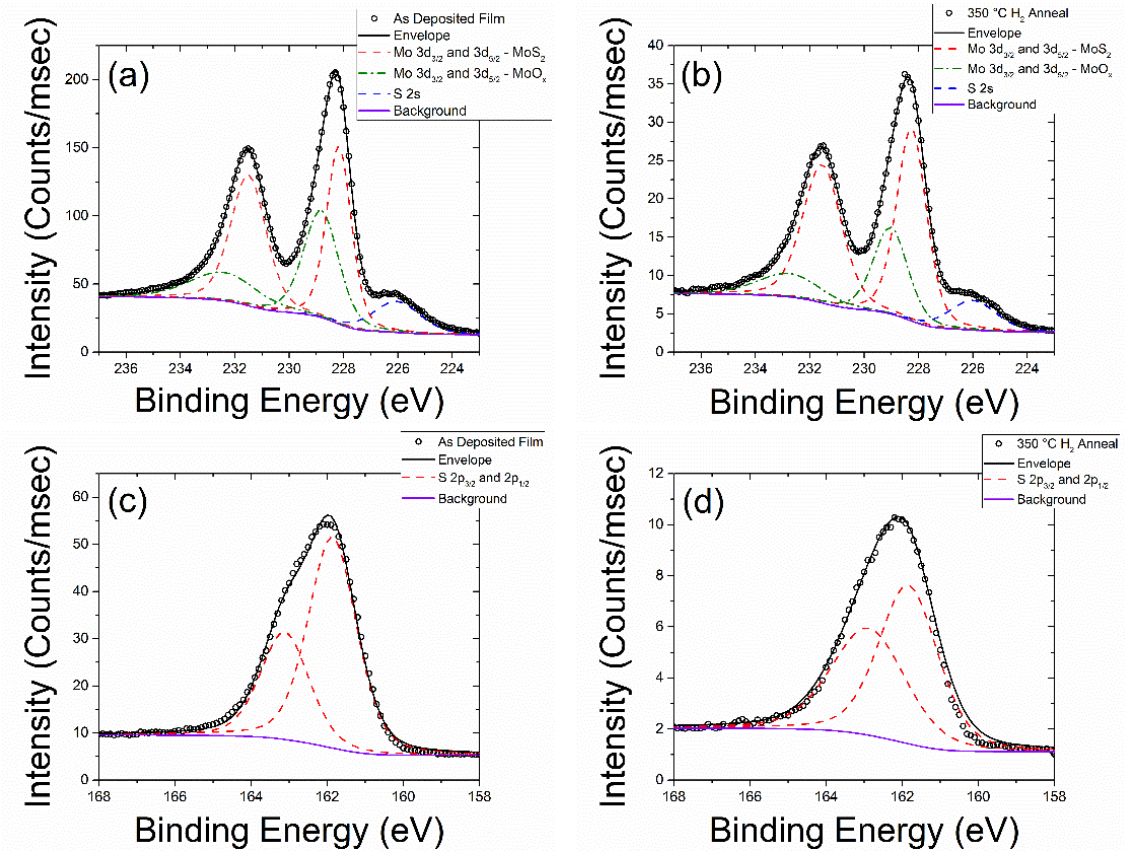

Fig. 10 High resolution scans of the (a) Mo3d region of the as-deposited, (b) Mo3d region of the annealed films, (c) S2p region of the as-deposited, and (d) S2p region of the annealed films.

XPS analysis can reveal the chemical makeup and atomic environments of the film surface. High resolution scans of the Mo 3d and S 2p regions for the as-deposited and annealed films are plotted in Fig. 10. Characteristic peaks associated with MoS_2 and MoO_x species were observed. The calculated Mo:S ratios for the as-deposited and annealed films were 1.1 and 1.35, respectively. The over-all composition of as-deposited and annealed films is shown in Table 4.

Table 4 Atomic percentages of the as-deposited and annealed films from XPS.

Sample	Mo	S	F	O
As-deposited	34.03	37.61	4.37	16.32
350 °C Anneal	36.54	48.9	1.22	12.7

The high oxygen content was attributed to removing the samples from the reaction chamber at the growth temperature (200 °C). MoO_x species are relatively stable up to 550 °C [74]. After analysis of the high-resolution Mo 3d peak envelope (Fig. 10(a) and Fig. 10(b)), the integrated peak areas of the peaks corresponding to the spin-orbit split $3d_{5/2}$ and $3d_{3/2}$ contributions for MoS_2 (~228 and ~231, respectively) relative to the neighboring S-Mo-O_x/Mo-O_x doublet (~229 and ~232 eV, respectively) in the as-deposited and annealed samples increased by 36% and 50%, respectively. Examination of the high-resolution S 2p peak envelope for both the as-deposited (Fig. 10(c)) and annealed samples (Fig. 10(d)) demonstrates the presence of only S^{2-} with spin orbit split $2p_{1/2}$ and $2p_{3/2}$ contributions arising at 162.9 and 161.7 eV, respectively. It can be concluded that, in addition to removing residual F arising from the MoF_6 precursor, annealing in H_2 removed some of the oxygen from the stable Mo-S_x-O_y phase, which yielded a purer distribution of MoS_2 with more dominant contributions attributed to Mo(IV) in the Mo 3d region. Thus, the higher relative amount of MoS_2 after annealing the films in H_2 at 350 °C. This result and the appearance of the (002) diffraction peak in the XRD pattern (Fig. 9(b)), support the formation of layered MoS_2 [73].

The XPS data also suggest that we are growing through the direct route, rather than the in-direct route. This suggestion does not explain the lack of a Raman signal, but if the crystal is highly disordered then the vibrational modes may be weak and broad. The lack of a Raman signal has been seen previously in sputtered MoS_2, but after an electron beam irradiation step, the fundamental Raman peaks appeared [75].

The optical band gap was determined from UV-vis measurements. 12 nm, 32 nm and 60 nm films were grown on fused silica substrates. One side of the substrate was

masked off with Kapton tape to prevent growth. The measurements were made in transmission mode, utilizing a total integrating sphere. Fig. 11(a) shows the transmission measurements of the 12 nm, 32 nm and 60 nm films. To determine the optical band gap, a Tauc plot [76] was constructed by converting the wavelength to eV and then using Eq. 16 to scale the transmission data. α is the absorption (1/transmission), $h\nu$ is the light energy, n is either ½, 2, 3/2 or 3 depending on the band gap transition, and E_g is the optical bandgap (x axis intercept).

$$(\alpha h\nu)^{1/n} = A(h\nu - E_g) \qquad \text{Eq. 16}$$

The constant, A, is material dependent with units $cm^{-1}eV^{-1}$ and can be is formally defined as:

$$A = (e^2 m p^2 V_{cell}/2\pi c\hbar^5 n)(m_v m_c/m^2)^{3/2} \qquad \text{Eq. 17}$$

where, e is the fundamental charge, m is the mass of an electron, p is the optical matrix element, V_{cell} is the unit cell volume in Å, n is the index of refraction, and m_v and mc are the density effective masses at the conduction and valence bands [77]. This was simplified by assuming $p \approx h/a$, where a is the lattice parameter, and that $m_v=m_c=m$ [77]. Tauc found good agreement with this simplification of Eq. 17 and experimental values reported by Davis *et al.* [78]. Using the crystalline approximations of the 2H structure of MoS_2, the plot in a line was fit to the 12 nm film in Fig. 11(b). Using this Tauc plot the band gap was determined to be 1.34 eV. This matches well with the bulk values of MoS_2 [79].

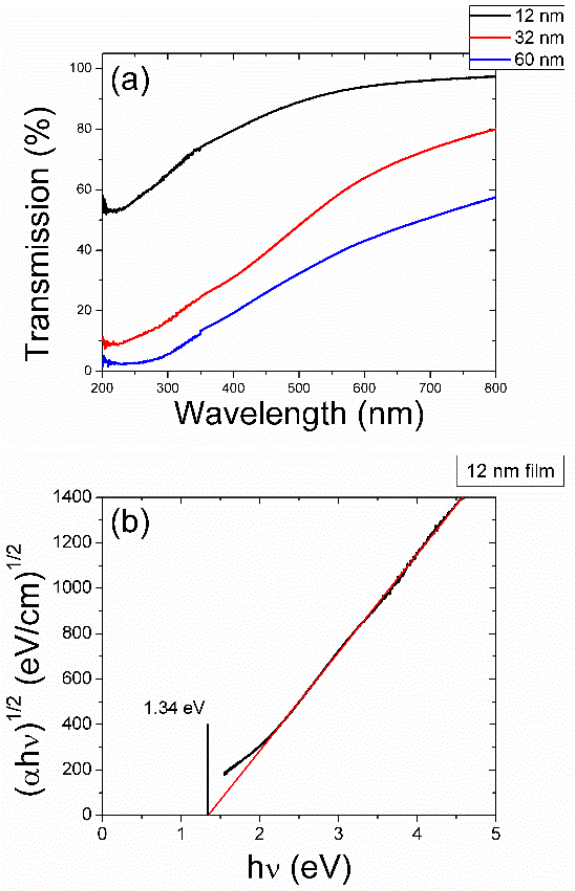

Fig. 11 UV-vis measurements of MoS_2 on fused silica substrates. Samples were measured in a transmission geometry of various thickness (a). Fitting a line to the 12 nm samples, the optical band gap was determined in the Tauc plot.

Conclusions

In this work, the growth of ALD MoS_2 was shown using MoF_6 and H_2S. Two growth routes were proposed: direct and in-direct. The direct route consisted of the formation of MoS_2 directly with the by-products of elemental sulfur and HF, while the in-direct route involved the formation of MoS_3 as an intermediate step requiring an annealing step in H_2 to reduce the MoS_3 to MoS_2. QCM studies showed that the in-direct method could not adequately explain the mass changes seen on the QCM as the mass ratios of the individual ALD cycles did not match the values for MoS_3 formation. In addition, XPS measurements did not find evidence of MoS_3 in the films but found MoO_x

species that were mainly attributed to the removal of the samples from the reactor at the growth temperature (200 °C). MoO_3 and MoO_2 species are quite stable at low temperatures and are difficult to remove once formed even in a reducing environment. However, using optical measurements, the optical band gap was found to be ~1.3 eV. This measurement matches bulk MoS_2, suggesting the MoO_x species are forming on the surface.

CHAPTER FOUR: NUCLEATION OF MOS_2 ON ALUMINUM OXIDE

Large scale fabrication processes of MoS_2 involve high temperatures and non-conventional substrates [80]–[82]. Field effect transistors (FETs), which are at the heart of microelectronics, have been fabricated using mechanically exfoliated MoS_2 in both top-gated and bottom-gated geometries [7], [8], but mechanical exfoliation is not scalable for manufacturing. These devices require the semiconducting material to be separated from the conductive gate by an insulation layer, which influences the carrier concentration depending on the applied bias [83]. To make thinner devices, the insulating layers above and below the semiconductor must have a high dielectric constant. This 2D material-dielectric interface is very sensitive to the underlying surface, [84] and on c-sapphire, can even cause anisotropic transport properties [85]. Moreover, making an Ohmic contact even becomes difficult because of an increase in trapped states, however introducing graphene and exotic metals has reduced contact resistances [86], [87]. In all cases, understanding the 2D material interface is crucial as this can affect device performance.

A monolayer of MoS_2 is approximately 0.6 to 1 nm thick [70]. Thus, only a small number of ALD cycles are needed to grow the film. Previous work reported a growth rate of 0.42Å/cycle using MoF_6 and H_2S [65], which equates to approximately 23 cycles. Many ALD chemistries have incubation periods or form some interphase during the beginning of the growth [20]. This could complicate the final chemistry of the film since this early growth regime and nucleation period becomes the final film in a single layer of

MoS_2. A better understanding of 2D interfaces for ALD MoS_2 is still needed if synthesis of wafer scale monolayer MoS_2 is to be achieved.

In this work, the nucleation and growth of MoS_2 on ALD Al_2O_3 are studied. Using *in situ* QCM and FTIR spectroscopy, the early growth regime was probed. A small incubation period occurs before MoS_2 starts to grow, and this incubation is temperature dependent. A growth mode was proposed during this early growth regime and measurements indicate Mo species readily bind with oxygen in the Al_2O_3. Reducing this effect could lead to cleaner MoS_2/oxide interfaces.

Experiment

ALD growth and *in situ* measurements were performed in a custom viscous flow reactor, which has been detailed previously [69]. Aluminum oxide was grown using trimethylaluminum (TMA, Strem Chemicals, min 98%) and de-ionized water. Molybdenum sulfide films were grown with (MoF_6, 98%, Sigma Aldrich) and hydrogen disulfide (H_2S, 99.5% Matheson Trigas, USA). The TMA and H_2O delivery pressures were controlled by needle valves, and the MoF_6 and H_2S were regulated using corrosive series regulators and 200 µm orifices.

Quartz Crystal Microbalance Experiments

Deposition of the films was characterized *in situ* using a QCM, which consisted of a modified Maxtek Model BSH-150 sensor head. A RC cut crystal with an alloy coating (Phillip Technologies) was used as the sensor due to its broad temperature range of stable operation. To prevent deposition on the backside of the crystal, silver paste was used to seal the crystal and sensor head, while the backside was purged with carrier gas. The reactor was kept at ~1 Torr by flowing ultra-high purity (UHP) argon.

When performing a QCM experiment, the reactor temperature was allowed to stabilize for six to eight hours in an attempt to reduce any frequency drift of the crystal. To keep the experiments consistent between temperature changes, 50 cycles of TMA and H_2O was deposited to encapsulate the system from the previous MoS_2 experiments. Typical recipes consisted of 50 cycles of the TMA and H_2O and ~20-40 cycles of MoF_6 and H_2S. An extra 30-second purge was added in between the TMA/H_2O and MoF_6/H_2S to reduce and risk of overlap.

in situ FTIR

For the *in situ* FTIR measurements, zirconia nanoparticles (Sigma Aldrich) were pressed into a 50 μm x 50 μm stainless steel mesh as the initial substrate. The nanoparticles are used to increase the optical absorption signal of the surface species. The mesh was mounted to a resistively heated sample holder and positioned in the beam path using a similar geometry as previously reported [88], [89]. During ALD depositions/dosing, gate valves in front of the IR windows were closed in order to prevent deposition on the KBr windows. [90]. Data acquisition was carried out using a Nicolet E700 FTIR from Thermo Scientific, and measurements were computer controlled after the purging steps. Like the QCM experiments outlined above, the substrate (ZrO_2 nanopowder) was coated with Al_2O_3 prior to the MoS_2 ALD. Because of the high surface area of the nanopowder, longer dose and purge times were used to sufficiently coat the powder. The pulse sequences are outlined for both the aluminum oxide and MoS_2 depositions in Table 5.

Table 5 Pulsing schemes for Al_2O_3 films grown on the ZrO_2 nanopowder and MoS_2 grown on the metal oxides for *in situ* FTIR measurements. ALD cycle pulses follow *Chemical A – Purge – Chemical B – Purge*.

Precursors	Film	ALD Cycle Pulse Sequence (sec)
TMA + H_2O	Al_2O_3	20 – 60 – 20 – 60
MoF_6 + H_2S	MoS_2	10 – 90 – 10 – 90

During the initial coating of the particles, FTIR measurements were recorded every five cycles. About 20 cycles of TMA and H_2O were needed to coat the nanoparticles and to achieve a symmetrical OH and CH_3 ligand exchange signal, which indicated complete Al_2O_3 coverage [91].

Thin Film Growth and Characterization

For XPS and TEM cross sections, 200 cycles of TMA and H_2O were deposited on clean silicon wafers at 200 ℃. 20 mm x 100 mm cleaved pieces of oxide film was loaded into the reactor and 50 cycles of MoS_2 was deposited on the surface. This was repeated at 150, 200, and 250 ℃. Prior to removal, the reactor was cooled to approximately 50 ℃ to minimize sample oxidation.

X-ray photoelectron spectroscopy (XPS) was performed on a Thermo Fischer K-Alpha+. XPS data was analyzed using Thermo Scientific Avantage software and all spectra were referenced to the C1s peak (284.8 eV). Fitting of the 2p and 3d peaks was constrained according to the spin-orbit split doublet peak areas and FWHM according to the relevant core level using a 30% mixed Gaussian-Lorentzian peak shape.

TEM images of the films were taken on a field emission JEOL JEM-2100F and FEI Tecnai F20. “Lift-out” samples were prepared using a Zeiss XB-1430 Focused Ion Beam Scanning Electron Microscope (FIBSEM). Prior to acquiring the images, the

substrate (sample) was used to align the Si substrate $[100]_c$ crystal direction with the optical axis of the TEM to ensure the interface alignment was correct.

Results and Discussion

Raman Spectroscopy Measurements

Raman spectroscopy is a common characterization technique for 2D materials. In layered form, these materials exhibit two fundamental vibrational modes, which have been used to determine the number of layers [70]. However, as seen in the measured Raman spectra in Fig. 12, the three as-deposited films did not show any characteristic peaks, similar to previous work [65], [66]. While not unexpected, these results indicate that MoS_2 ALD at 150 and 250 ℃ yield amorphous films, similar to the 200 ℃ growth Chapter 3.

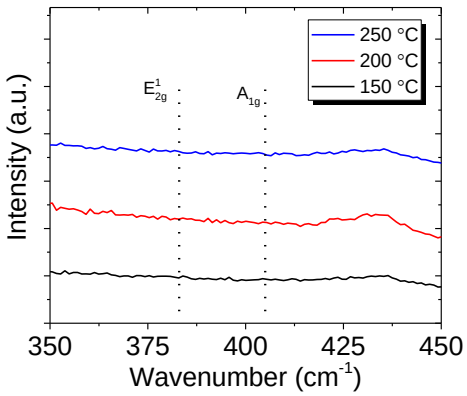

Fig. 12 Raman spectra of 50 cycles of MoS_2 on ~20 nm of ALD Al_2O_3 at 150, 200, and 250 ℃. Dotted lines show where bulk modes should appear for layered MoS_2. The data have been offset for clarity.

Quartz Crystal Microbalance Measurements

QCM allows for the measurement of small mass changes on the sensor's surface by monitoring the frequency shifts of the resonating crystal. The mass change can be related to the frequency shift using the Sauerbrey equation:

$$\Delta m = -\frac{A\sqrt{\rho_q \mu_q}}{2f_0^2}\Delta f, \qquad \text{Eq. 18}$$

where Δf is the observed frequency change in Hz, Δm is the mass per unit area in g/cm^2, f_0 is resonant frequency, A is area of crystal, ρ_q is the density of quartz, and μ_q is the shear modulus of quartz. QCM systems typically use an internal reference crystal to determine the frequency offset and compute the mass change of an absorbing atom or molecule [92]. QCMs are extremely sensitive and are able to resolve sub-nanogram changes in mass with millisecond time resolution. This allows for not only the over-all mass of an ALD cycle to be determined, but also any absorption and desorption of chemical species.

Multiple TMA and H_2O ALD cycles were repeated on the QCM crystal until the measured mass change after each complete ALD cycle was consistent. This mass change per cycle (MCPC), representing the net change after a complete AB cycle, MCPC) can be used as an indicator for determining when steady state growth is achieved, and for TMA and H_2O this has been well characterized [20]. MCPCs of 36, 41, and 38 ng/cm^2 were measured at 150, 200, and 250 ℃, respectively, and match the literature value of 40 ng/cm^2 for TMA and H_2O [20].

Fig. 13(a) plots the mass changes observed for the first two cycles of MoF_6 and H_2S at 150, 200, and 250 ℃ on the ALD Al_2O_3 coated quartz crystal. The time and duration of each precursor dose is illustrated at the bottom of the plot. In this experiment, the first pulse was MoF_6, which has been set as time equals zero. The sharp mass increases in Fig. 13(a) result from MoF_6 adsorbing onto the surface of the crystal. The gradual mass loss after this peak is caused by desorption reaction products or physisorbed MoF_6. The net mass change is determined once the mass signal has stabilized. As seen in

Fig. 13(a), large net mass gains of 111, 85, and 67 ng/cm^2 for the 150, 200, and 250 ℃ growth temperatures were measured for the first dose of MoF_6. The temperature dependence of this mass gain is most likely from reducing OH surface species at elevated temperatures [93], since the OH coverage at the end of the ALD Al_2O_3 growth determines the density of reaction sites on the crystal. However, the differences in net mass change could also result from temperature-dependent precursor instabilities (e.g., decomposition and desorption). At 150 ℃, the mass loss was approximately twice as large as that at 200 and 250 ℃. This change could indicate that below 200 ℃ adsorbed species do not have the energy to leave the surface.

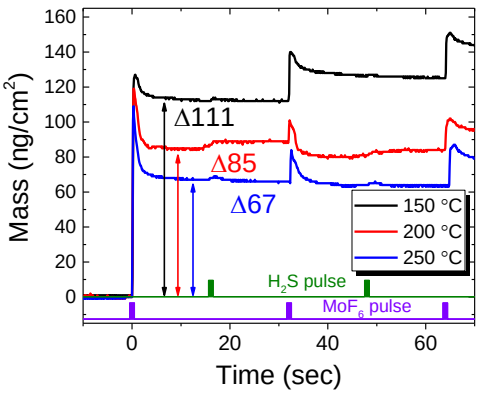

Fig. 13 QCM measurments showing the measured mass changes for the first two cycles of MoS_2 on the Al_2O_3 coated crystal.

Interestingly, after the H_2S doses (~18 and 48 seconds), little to no net mass change was observed. Additionally, the mass change after the second MoF_6 dose is significantly less for all temperatures. The lack of mass change after the H_2S and the reduced MoF_6 mass gains suggest that after only one ALD cycle, the surface chemistry has changed significantly from the initial Al_2O_3 surface.

To better understand what should be expected after the dose of MoF_6, the estimated maximum mass gain can be calculated using the average number of OH groups per unit area on Al_2O_3 [93].

$$\frac{\Delta M}{cm^2} \times \frac{1\ mol\ Al(CH_3)_{1.5}}{50 \times 10^9\ ng} \times \frac{1\ mol\ Al}{1\ mol\ Al(CH_3)_{1.5}} \times \frac{1\ mol\ OH}{1\ mol\ Al} \times \frac{6.022 \times 10^{23}}{1\ mol\ OH} = [OH]/cm^2 \quad \text{Eq. 19}$$

Experiments have found that on average TMA loses 1.5 of its 3 methyl groups every ALD cycle [94]. Using 40 ng/cm^2 for mass change (ΔM) and the molar mass of the chemisorbed TMA, the OH concentration was calculated to be 5.7×10^{13} [OH]/cm^2. Again, if every MoF_6 molecule interacts with every OH group and forms molybdenum oxyfluoride (more details on this decision will be discussed later), the estimated mass gain, ΔM_{MoF6} equals:

$$\frac{5.7 \times 10^{13} OH}{cm^2} \times \frac{1\ mol\ MoF_4O}{OH} \times \frac{158 \times 10^9\ ng}{1\ mol\ MoF_4O} \times \frac{1\ mol}{6.022 \times 10^{23}} = \Delta M_{MoF6}\ (ng/cm^2) \quad \text{Eq. 20}$$

Like the experimental results, Eq. 20 equals approximately 150 ng/cm^2. This is larger than any mass gains observed during the first cycle in Fig. 13. However, the over estimation is expected as some binding sites may be blocked due to steric hindrance or from reaction with F liberated by the Mo precursor [20]. Previous experiments have shown the hydroxyl density on ALD Al_2O_3 decreases gradually as the growth temperature is increased, at 250 ℃ the OH concentration is about half of the amount at 150 ℃ [93]. This reduction in surface reaction sites provides a plausible explanation for the observed decrease in mass gains observed for the first MoF_6 pulse, seen in Fig. 13, as the growth temperature is increased. The QCM data and calculations suggest that during the initial dose of MoF_6 any available OH binding sites are consumed. Using this as a

proposed reaction mechanism, the possible surface species relevant for the reaction between MoF_6, ALD Al_2O_3, and by-product interactions can be hypothesized.

$½Al_2O_3 + 3HF(g) \rightarrow AlF_3 + 3/2H_2O(g)$	ΔG = -122 *kJ/mol*	Eq. 21
$Al(OH)_3 + MoF_6(g) \rightarrow AlF_3 + MoO_3 + 3HF(g)$	ΔG = -357 *kJ/mol*	Eq. 22
$⅓Al(OH)_3 + MoF_6(g) \rightarrow ⅓AlF_3 + MoOF_4 + HF(g)$	ΔG = -158 *kJ/mol*	Eq. 23
$Al(OH)_3 + 3HF(g) \rightarrow AlF_3 + 3H_2O(g)$	ΔG = -127 *kJ/mol*	Eq. 24
$MoF_6(g) + 3H_2O \rightarrow MoO3 + 6HF(g)$	ΔG = -198 *kJ/mol*	Eq. 25

Thermodynamic calculations of the free energy of reaction made in HSC Chemistry are shown in Eq. 21 - Eq. 25 [71]. Because aluminum fluoride (AlF_3) is a stable compound and is relatively easy to form when Al_2O_3 reacts with HF gas (Eq. 21) [95], it is assumed when MoF_6 and Al_2O_3 react, the fluorine will want to bind to the Al over the Mo. The formation of AlF_3 and MoO_3 (Eq. 22) has the largest negative energy of reaction of -357 kJ/mol of the proposed reaction routes. This high reaction energy is not unexpected as MoS_2 readily oxides, even at relatively low temperatures [74]. Additionally, reports have found a metal oxyfluoride species when metal oxides are fluorinated [96]. Assuming AlF_3 again forms, Eq. 23 is also a probable surface species with a ΔG of -158 kJ/mol. Because hydrogen fluoride is a by-product for MoF_6 and H_2S [65], this too could interact directly with the Al_2O_3, producing water (Eq. 24) that can decompose the MoF_6 precursor (Eq. 25). All of these proposed surface interactions suggest a high probability that the interface, or even the first few cycles will have a large oxygen content. In addition, these proposed reactions suggest that the Al-OH surface is changing to an Al-F surface, reducing the reactivity, which is observed as a decrease in the MCPC after the first ALD cycle.

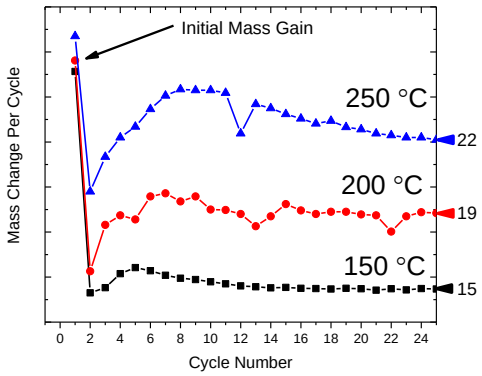

Fig. 14 The mass change per complete AB cycle for each growth temperature is plotted for the first 24 cycles. The plots have been offset vertically with the steady state mass change indicated to the right of the axis.

In Fig. 14, the total net mass change for each complete MoF_6/H_2S ALD cycle is plotted. In the first cycle, as described above, a large increase in mass was observed followed by a smaller mass change for the second cycle. This behavior is attributed to a change in surface chemistry. After the first two cycles, the MCPC steadily increased to a maximum and extended over a larger number of cycles as the growth temperature was increased. At 200 °C, our observed MCPC agrees with the value reported by Mane *et al.* of approximately 20 ng/cm^2/cycle [65]. At 150 °C, a lower steady state MCPC of 15 ng/cm^2/cycle was observed after approximately 12-14 cycles, while at 250 °C, it takes about 22-24 cycles to reach a higher steady-state MCPC of 22 ng/cm^2/cycle. Islanding of MoS_2 on the Al_2O_3 could explain this, as the surface area of the crystal essentially increases (i.e. higher mass gains per cycle), thus overestimating the MCPC. At higher temperatures, nucleation will occur faster (more thermal energy); however, the density of binding sites is also lower. This suggests that binding site concentration dominates the nucleation and growth rate is reduced on an Al-F terminated surface.

Fourier Transform Infrared Measurements

FTIR can give insight into the bonding and certain surface species that are present. The technique has been coupled with the ALD reactors, so absorption spectra can be obtained between individual half cycles. Previously, *in situ* FTIR of TMA and H_2O ALD has been demonstrated [88]. Difference curves of the absorption spectra show a "flip-flop" caused by changes in surface species between hydroxyls (3200 to 3700 cm^{-1}) and methyl groups (3000 cm^{-1}) (as previously discussed in Eq. 3 and Eq. 4). Difference curves are constructed by subtracting a prior absorption spectrum to a spectrum of interest, thus highlighting any changes that occurred between the two spectra. Fig. 15 shows the FTIR difference plots (red and black) of the last cycle of TMA and H_2O prior to beginning the MoS_2 ALD at 150, 200, and 250 ℃. The inverse signals are indications of steady state growth. Difference curves for the first and second MoF_6 and H_2S doses are shown in Fig. 26 for growth at 150, 200, and 250 ℃. The lower panels show the lower frequencies where bulk modes of the metal atoms are present.

At each temperature, upon MoF_6 exposure to the OH-terminated Al_2O_3 surface, a clear decrease in the Al-O bulk mode peak from 1000 to 800 cm^{-1} is observed in Fig. 15, suggesting the consumption of Al-O bonds. Interestingly, no Al-F peaks were observed, which occur below 800 cm^{-1} [97]. Al-F species are predicted by Eq. 22 and 23. However, in highly disordered AlF_x films, all vibrational modes become active, broadening Al-F peaks [97]. This would essentially spread out any intensity over a larger range and make the signal difficult to observe. Moreover, the reactions are limited to a thin surface passivation [95] meaning no bulk modes would be present. Thus, Al-F species may be forming below the detection sensitivity of the experiment.

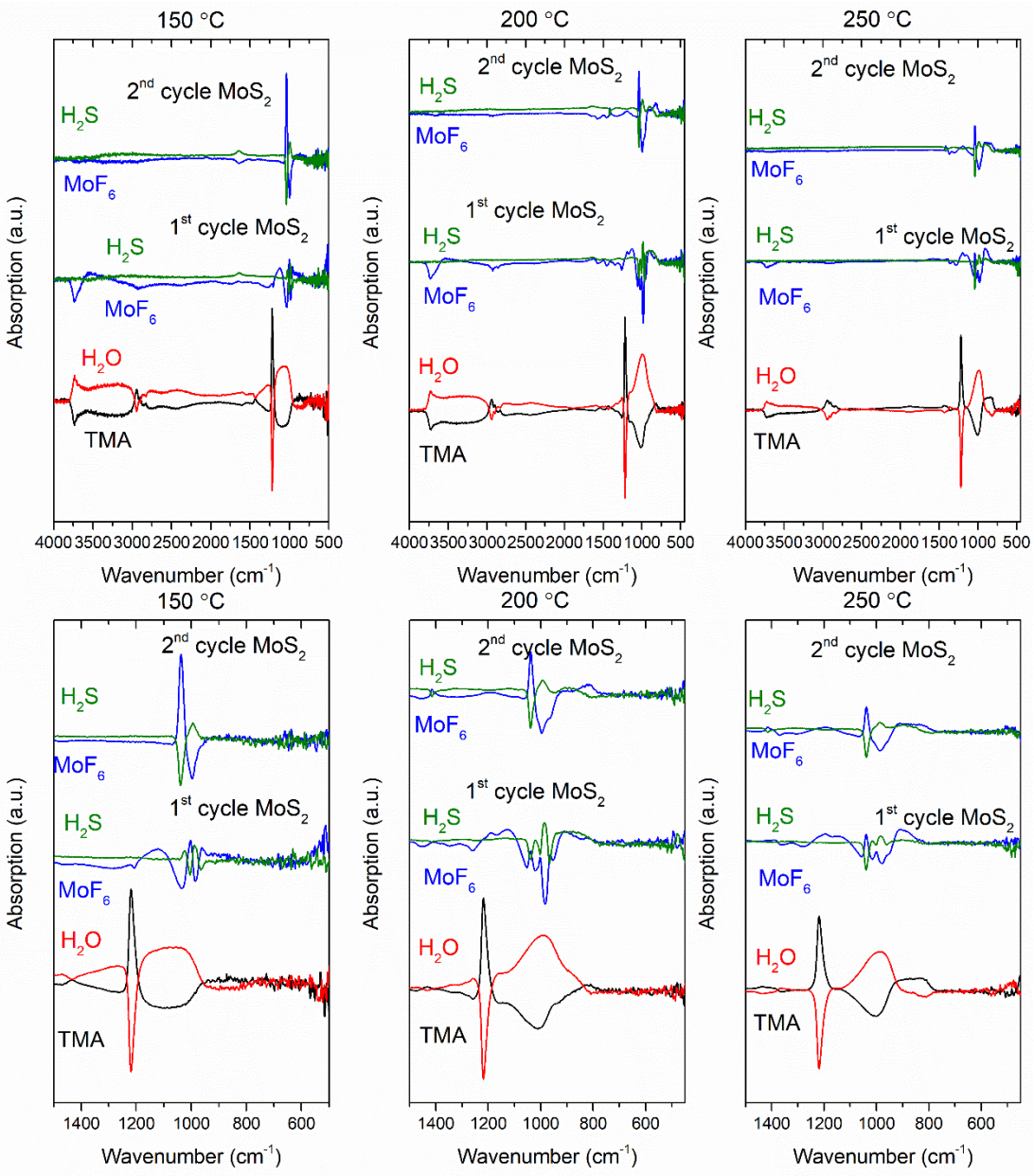

Fig. 15 FTIR data of the first two cycles of MoS_2 deposited on ALD Al_2O_3 for 150, 200, and 250 °C. Plots on top show the full range, where the OH stretches of the last water pulse (in red) can be seen above 3500 cm^{-1}. The lower plots show the lower frequencies where bulk modes of the metal atoms are present. The absorption scale was adjusted for each data set to maximize the peak heights and the y-axis scale varies between plots.

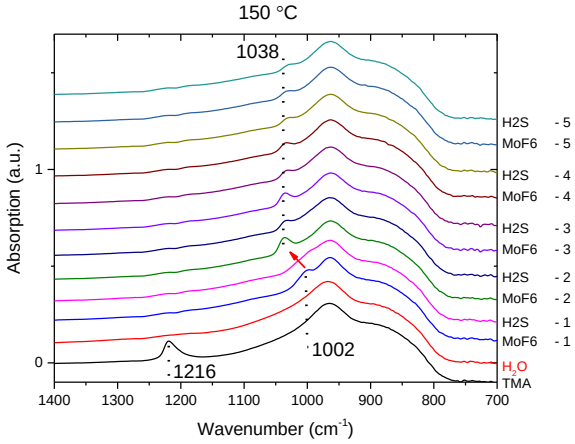

(a)

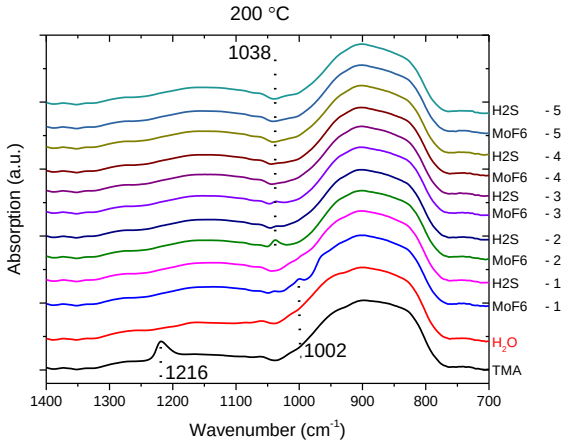

(b)

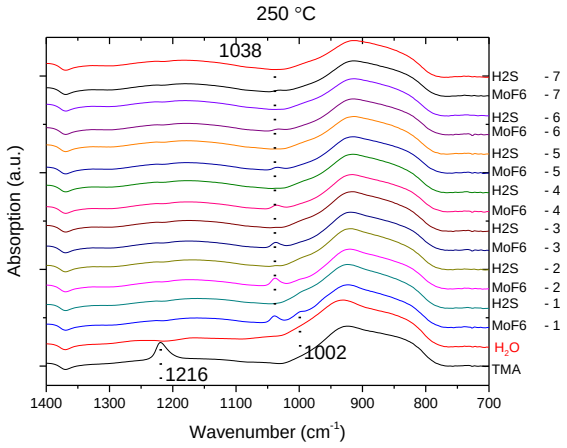

(c)

Fig. 16 FTIR absorption measurements at (a) 150 °C, (b) 200 °C, and (c) 250 °C. In each, the first two spectra, in red and black, are the last TMA and H_2O ALD half-cycles. Subsequent cycles numbers are labeled to the right of the axes. Dotted lines indicate key features: C-H bending mode at 1216 cm^{-1}, Mo=O stretch in MoF_4O at 1038 cm^{-1}, suspected Al-F species at 1002 cm^{-1}.

The difference curves in Fig. 15 can become difficult to interpret when there are shifts in intensity of broad peaks. These shifts can be observed more clearly in the total absorption spectra data (Fig. 16). After the initial MoF_6 pulse, a peak at 1002 cm^{-1} is observed, which disappears after the first cycle. After the MoF_6 dose of the second ALD cycle, a peak at 1038 cm^{-1} is observed. After analysis of the 150 and 200 ℃ experiments, the two peaks were initially thought to be caused by the same surface species and simply shifting in frequency. However, at 250 ℃ both peaks are visible after the first cycle suggesting they are from two separate surface species. It would seem plausible to associate the 1002 cm^{-1} peak to an Al-F stretch, but to-date we have been unable to identify a surface species predicted in this range. AlF_3 and Al_2F_6 *gas phase* species have been reported in this range [98], however further studies will be needed to confirm if the peak arises from Al-F stretches. Future isotopic labeling experiments with heavy oxygen could give insights into the peak's origins. Regardless, these two peaks again suggest that the very first cycle is changing the surface chemistry for subsequent ALD cycles. The peak that persists and appears after the second dose of MoF_6 at 1038 cm^{-1} matches the Mo=O stretch in $MoOF_4$ [96]. Moreover, ALD isotopic experiments using both, oxygen-18 labeled H_2O and non-labeled H_2O, a peak shift was observed at 1038 cm^{-1} [99]. This would suggest that the peak is associated with the oxygen bonding state.

After each H_2S dose, the $MoOF_4$ peak disappears, which is seen as a negative intensity in Fig. 15. Unfortunately, our experimental set-up was spectrally limited, and unable to see below ~525 cm^{-1} where many of the Mo-S modes [100] are located. This made it difficult to conclude if any Mo-S bonds were forming at the expense of the $MoOF_4$ peak. After multiple cycles of MoS_2, an increase in baseline of the absorption was

observed, as seen in Fig. 17. This is attributed to the absorption of light from free carriers in the MoS_2 semiconductor. A horizontal line was fit to the background in a featureless region from 1675 to 1725 cm^{-1}. For each temperature, the y-intercept of the horizontal line fit to each spectrum was plotted in Fig. 18. For completeness, the last TMA and H_2O half-cycles were included at the beginning of Fig. 18. Little change to the baseline was observed for about six cycles for all growth temperatures. After this small incubation period, a linear increase in the baseline was observed, where the MoS_2 is forming. Once the baseline began to increase linearly, the absorption would oscillate between the MoF_6 and H_2S doses. On the MoF_6 doses, the baseline would decrease, while after the H_2S pulses the baseline would increase. This indicates the film is becoming more conductive (an increase in free carriers) during the H_2S pulses, suggesting that the reaction is forming MoS_2 as early as 6 cycles after growth.

This incubation period correlates closely to the loss of the $MoOF_4$ peak. In Fig. 16, the peak at 1038 cm^{-1} disappears after about 6 – 8 cycles, roughly correlating with the baseline increase, which is attributed to the growth of MoS_2. This suggests that once the reactions stop consuming oxygen (i.e., forming Mo=O bonds), Mo-S bonds start to form. When $MoOF_4$ forms, the double bond replaces two fluorine atoms on the MoF_6 molecule. However, sing the mass ratio calculations of the direct method (Eq. 11), no loss of fluorine was observed in the QCM measurements during steady state growth. If $x = 2$ in Eq. 11, MoF_6 would lose two F atoms during the first half-cycle causing the mass ratio, $R = 1.06$, which is close to unity. For reference, the mass ratio is the molar mass of the surface species in first cycle, Δm_a, divided by the overall molar mass deposited on the surface, Δm:

$$R = {\Delta m_a}/{\Delta m} = {(210 - 20x)}/{160}. \quad \text{Eq. 26}$$

This result is consistent with the MoF_6 half cycle contributing the most to the mass change and the H_2S half cycle showing a near zero mass change seen in Fig. 13. A consequence of this is that the oxygen reaction with Mo during this early growth seems to dominate the growth. As MoO_x species are undesirable because of its large band gap, minimizing this effect is key to developing a high quality film. Using a barrier layer or non-oxygen containing substrate will be needed to form a high quality interface. This adds an extra layer of complexity when fabricating devices, as many of the high-k materials used in devices are metal oxides.

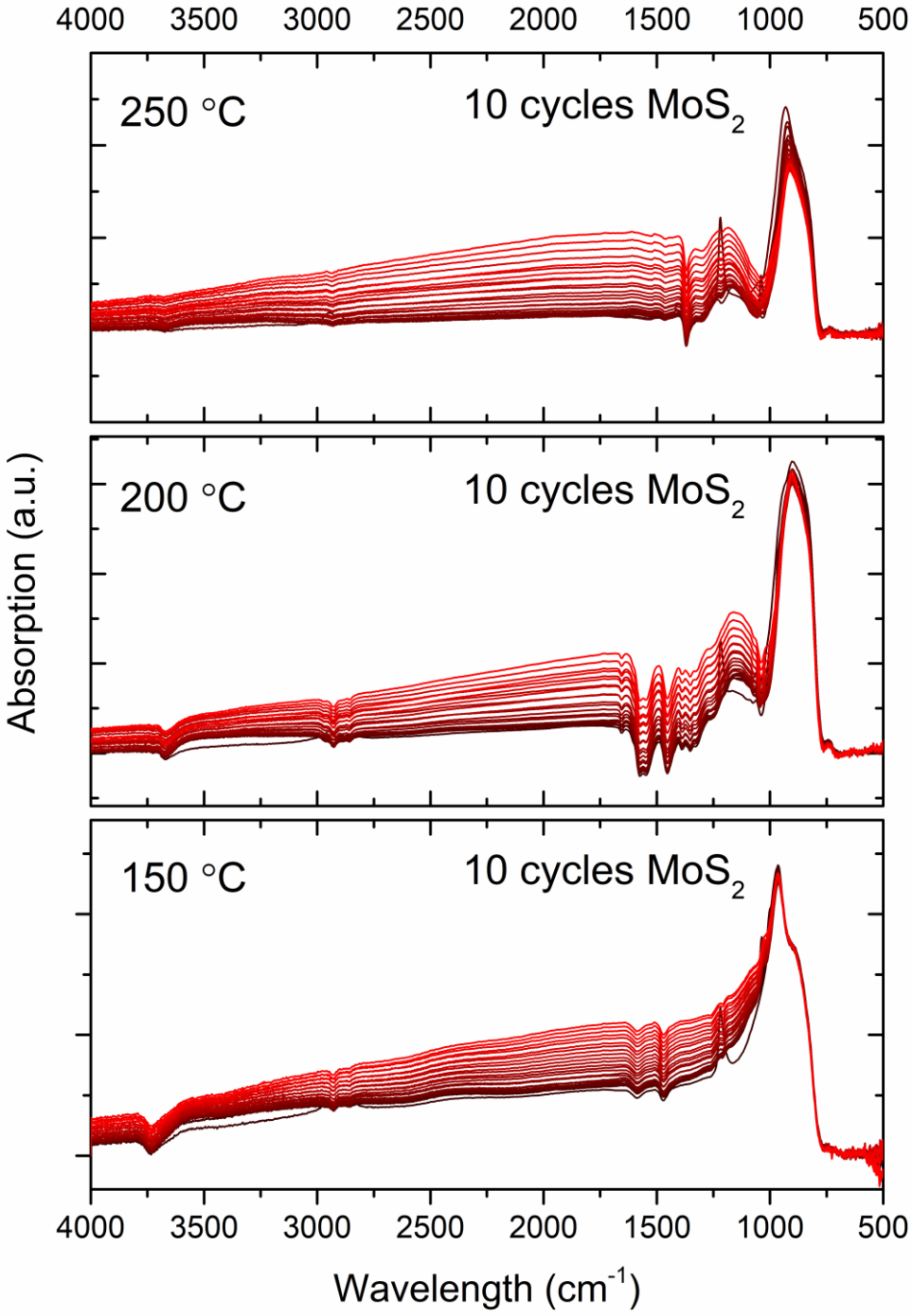

Fig. 17 Absorption spectra of MoS_2 deposited on ALD Al_2O_3 at 150, 200, and 250 °C. Darker colors (starting with black) indicate early cycles, while red colors indicate the later cycles.

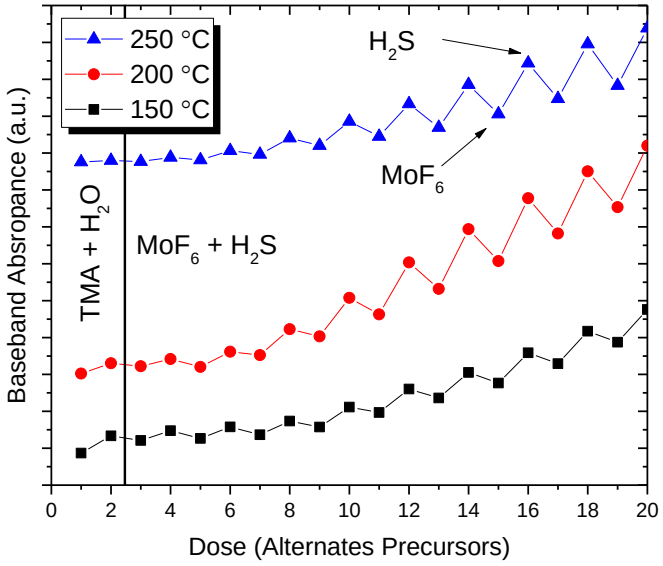

Fig. 18 A plot showing the baseline value for 10 cycles of MoS_2. The baseline was determined by the Y-intercept of a horizontal line fit to 1725 to 1675 cm^{-1} at each temperature. Each data point represents a single half-cycle of the AB chemistry. For consistency with the other plots, the first two data points are from the last TMA and H_2O ALD half-cycles, while all others are alternation MoF_6 and H_2S.

Film Characterization

High resolution XPS measurements of the Mo 3d and S 2p regions of the as-deposited films at 150, 200, and 250 ℃ are shown in Fig. 19. Oxygen species were found at all growth temperatures. This result was expected after the above FTIR analysis and previous reports [65]. At 150 ℃, the film contains only ~7 % MoS_2 with the rest of the film being a MoO_x species. This film seemed to contain the least amount of MoS_2, which could indicate we are below an energy barrier for the formation of MoS_2 on the surface. Thermodynamic calculations could not explain this; however, perhaps ab-initio modeling could give insight into how the temperature is affecting the growth. The 200 ℃ sample had a larger MoS_2 percentage, near 66 percent. Two sulfur environments were clearly present in the S 2p region. While the doublet at ~161.9 eV is associated with the S^{2-} of

MoS_2, the second shifted higher doublet could be clusters as will be discussed in Chap. 5. The Mo:S ratio was calculated using the area of the S $2p_{3/2}$ spin doublet, at 167.8 eV, divided by the Mo $3d_{5/2}$ spin doublet at 229.5 eV. This Mo:S ratio was approximately ~1.5, which is sub-stoichiometric, but an improvement over previous results at this temperature [65]. The 250 ℃ was more complicated to deconvolute because the need of a third doublet to properly model the envelope. XPS of sub-stoichiometric molybdenum oxysulfides were measured by Benoist *et al.*, who needed a similar treatment of the their films [101]. The doublets at 229.8 and 231.95 eV are near MoO_2 and MoO_3 species, but shifted to a lower energy, which could arise from disorder [101]. Using the same quantification methods as the 200 ℃ samples, the Mo:S ratio of the MoS_2, increased to 1.85 in these films. Although an improvement, this is overshadowed by the large amount of oxide phase. High temperature annealing could be used to try to convert these oxide interfaces into MoS_2; however, reducing or eliminating oxygen from the nucleation surface could also be effective.

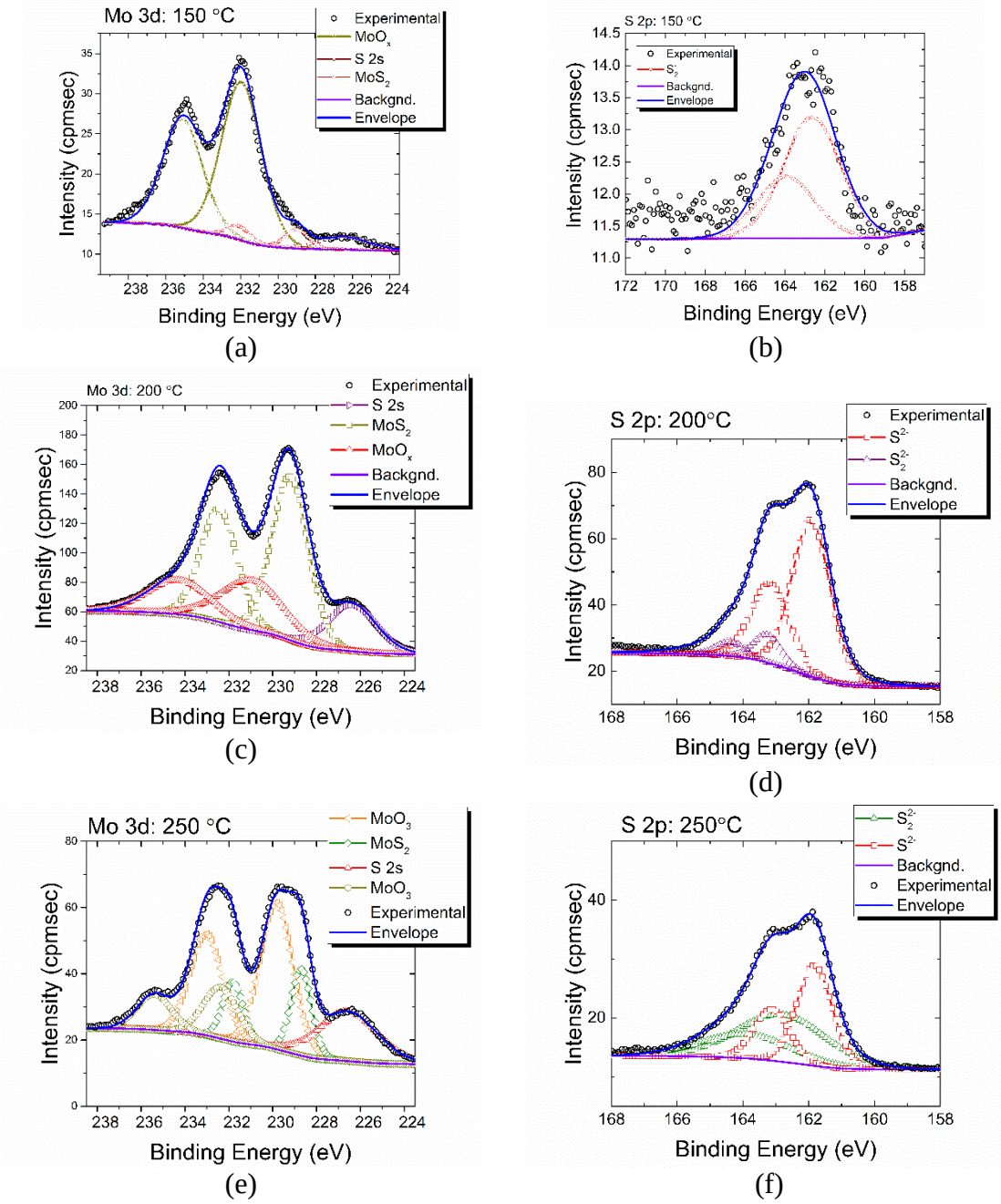

Fig. 19 High resolution XPS scans of the Mo 3d and S 2p regions of 50 cycles of MoS_2 deposited on ~20 nm ALD Al_2O_3 at 150 °C, 200 °C, and 250 °C.

To measure the film thickness, 50 cycles of MoS_2 was grown on ALD Al_2O_3 at 200 and 250 ℃ (Fig. 20). Because of the low MoS_2 quantity when grown at 150 ℃, the film was not included. As the growth temperature is increased, the MoS_2 film thickness decreases. At 250 ℃, the film is 1.5 nm thick, which equates to 0.02 Å/cycle and at 200 ℃ the growth per cycle (GPC), is 0.07 Å/cycle. These values are smaller than all previous work with MoF_6 and H_2S [65], [66]. The comparison of the 200 and 250 ℃ films is complicated by the difference in film thickness and the differing incubation periods, as see in Fig. 14. The differing thicknesses could also explain the high oxygen content of the 250 ℃ film. Assuming the photoelectron escape depth is the same, the sampling depth for the thinner film will be closer to the oxide interface. The 250 ℃ XPS scan could be a better representation of what the metal oxide interface chemistry is, however a thicker sample would need to be made before this could be confirmed.

The differences in film thickness are consistent with growth rates that greatly depends on the substrate's initial nucleation density, which we attribute here to the initial OH concentration on Al_2O_3. In contrast, the experiments described in Chap. 3 were completed using primarily silicon containing substrates, and Si is known to reduce MoF_6 quite readily [65], [68]. The experiments in Chap. 5, used high surface area hydroxylated carbon nanotubes [66], which we believe behaved similar to the OH-terminated Al_2O_3.

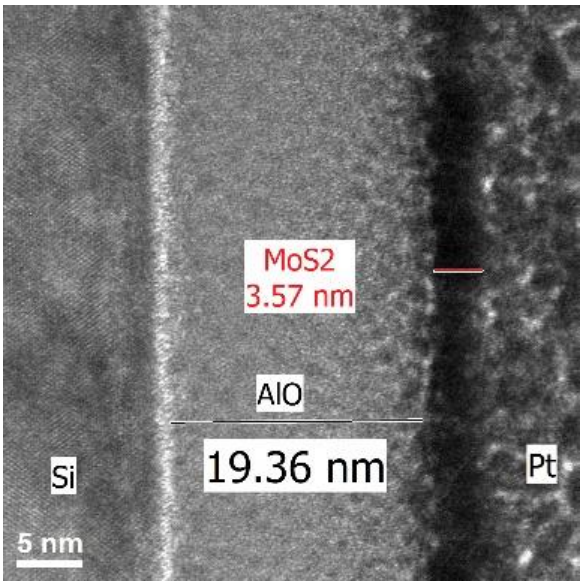

(a)

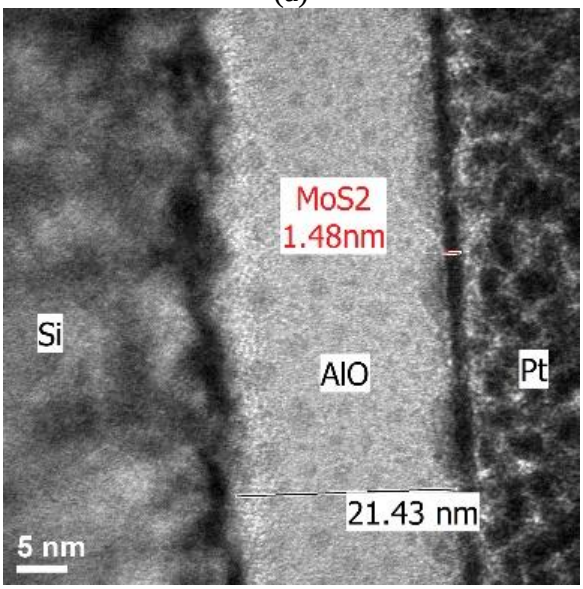

(b)

Fig. 20 Transmission electron micrscope images of cross-sections of as-deposited MoS_2 on ~ 20 nm of ALD Al_2O_3. The MoS_2 was deposited at (a) 200 ℃, and (b) 250 ℃.

Conclusions

We have shown that MoF_6 and H_2S grow MoS_2 on ALD Al_2O_3. Similar to our previous work, as-deposited films were amorphous and did not exhibit any MoS_2 fundamental Raman modes. Using *in situ* QCM and FTIR, the first few cycles were measured in an attempt to determine how the nucleation of MoS_2 begins. QCM

measurements predicted large mass gains if OH groups were the primary mode of growth, which was consistent only with the very first dose of MoF_6. Subsequent ALD cycles showed a much lower mass gain suggesting that OH groups are consumed during the first ALD cycle. Thermodynamic calculations predicted a complicated reaction between the Al-OH and MoF_6 precursor, which complicated understanding the first FTIR spectrum. After the first dose, a $MoOF_4$ peak was observed which was consumed when H_2S was introduced. The free carriers in MoS_2 increased the absorption and was observed as an increase in the baseline absorbance. Using this as an indication of growth, we determined the MoS_2 incubation period to be approximately 5 to 6 cycles on ALD Al_2O_3. The growth temperature heavily influenced the GPC of the film, suggesting that a higher growth temperature could help control thickness. Methods of reducing the path ways for $MoOF_4$ creation could lead to oxygen free interfaces and the ability for ALD of MoS_2 to be widely used in electronics.

CHAPTER FIVE: STRUCTURE OF ATOMIC LAYER DEPOSITED MOS_2

Early reports of the ALD of MoS_2 using various Mo and S precursors found that as-deposited MoS_2 films were amorphous, but annealing the films in an oxygen-free atmosphere at 800 ℃ produced layered films [44], [57], [62], [64]. Additionally, these reports found that when the ALD cycle number is low, the films did not exhibit the characteristic Raman signature of bulk MoS_2 [70]. Interestingly, after many ALD cycles, weak Raman peaks appeared, suggesting that a layered structure had formed in low concentrations or microcrystalline regions.

In this work, we aim to understand the local structure and degree of long-range coherence of the as-deposited ALD MoS_2 films in an effort to identify growth conditions to achieve ultrathin, crystalline MoS_2 directly by ALD at low temperatures. While electron microscopy has been used previously to study the structure of ALD MoS_2, only a small fraction of the sample volume is probed using this method [52]. Bulk characterization techniques have also been applied to as-deposited ALD MoS_2 films including X-ray photoelectron spectroscopy (XPS), benchtop X-ray diffraction/scattering, and Raman spectroscopy [70]. These techniques can give insight into the layered structure, but provide only limited structural information. Here, we use a combination of synchrotron-based X-ray absorption spectroscopy (XAS) and high-energy X-ray diffraction (HE-XRD) coupled with atomic pair distribution function (PDF) analysis with reverse Monte Carlo (RMC) modeling to understand the short-range and long-range order in as-deposited and annealed MoS_2 films.

X-ray Absorption Spectroscopy and High Energy X-ray Diffraction

XAS is a powerful tool for understanding local chemical environments and is used here to probe the oxidation state and coordination environment of Mo in ALD MoS_2 films. However, structural information from XAS is limited to the first coordination sphere of the probed element. The technique is relatively new but very powerful for amorphous materials. Using what is sometimes referred to as the "XAFS equation" [102], [103], shown in Eq. 27, this estimates the oscillations in the extended X-ray absorption fine structure (EXAFS) region normalized to background absorptions as a function of the wavevector, *k*.

$$\chi(k) = S_0^2 \sum_i N_i \frac{f_i(k)}{kD_i^2} e^{-\frac{2D_i}{\lambda(k)}} e^{-2k^2\sigma_i^2} sin\left(2kD_i + \delta_i(k)\right) \qquad \text{Eq. 27}$$

The equation gives the modification to the electron wave function at the origin of scattering by a neighboring atom, N_i, at a distance D_i. S_0^2 is the amplitude reduction factor, λ is the mean free path of the photoelectron, σ_i is the mean square displacement, which models thermal vibrations, and f_i is the proportionality constant as a function of *k*. Fitting of these peaks is accomplished by using a known crystal model, like structural data obtained from X-ray diffraction. Fig. 21 shows an illustration explaining the source of the X-ray absorption fine structure (XAFS) data adapted from *The Fundamentals of XAFS* by Matthew Newville [104]. When an absorbing atom produces a photoelectron, its wave function can be perturbed which will change how the neighboring atoms absorb energy. This happens on a macroscopic scale that gives rise to an average energy spectrum seen in blue (Fig. 21). The fluctuations are directly dependent on the structure of the material.

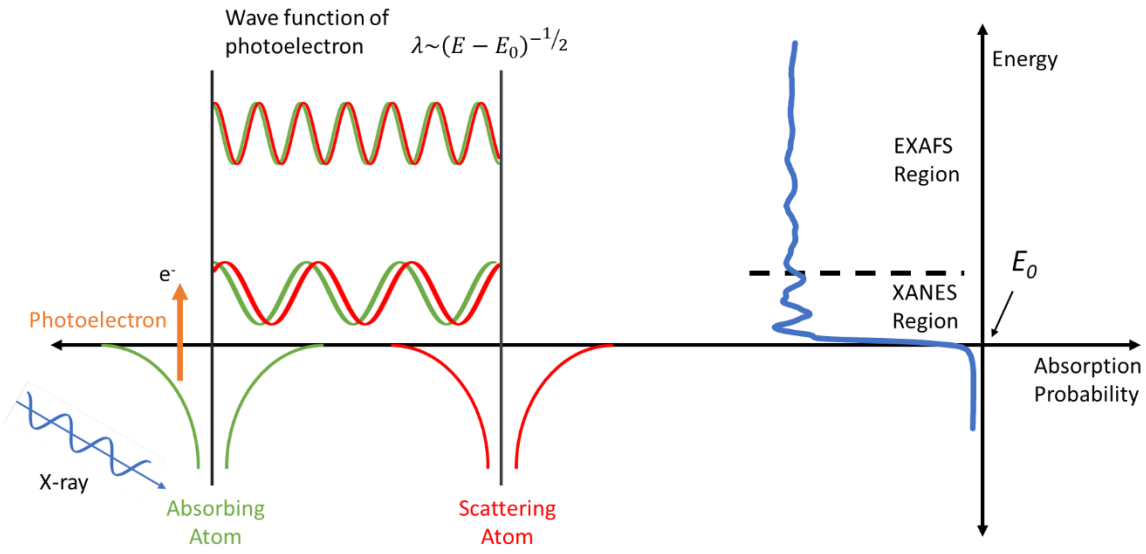

Fig. 21 Illustration adapted from *The Fundamentals of XAFS* [104], showing the electron wave function of an ejected photoelectron perturbed by a neighboring atom. This scattering atom causes an energy change to the absorption energy that is displayed as "wiggles" in the absorption edge. Typically, the data is split into two regimes: the XANES region, which includes the absorption edge and near the edge features, and the EXAFS region, which contains longer order structure and can be fitted to known crystal structures.

Ab-initio calculations can model all possible scattering paths for a crystal model and can be used to approximate the EXAFS regime [105]. To improve the accuracy, typically a standard is used to obtain the atom specific amplitude scattering factor, which can then be transferred to experimental environments [103].

XAS can be complemented with HE-XRD measurements and coupled with PDF analysis to provide longer-range structural information [106]. PDF analysis considers both the diffuse and Bragg components to provide detailed structural information, even in the absence of long-range structural coherence [107], [108]. PDF is especially useful for studying the atomic structure of amorphous and nanoscale materials, which inherently lack long-range order. In this work, analysis of the XAFS data helped determine the coordination around Mo-S and Mo-Mo pair peak, while PDF measurements and RMC

modeling provided key insights into the bond pairs of all atoms. In addition to examining the as-deposited films, ALD MoS_2 films were examined following annealing in reducing (H_2) and sulfurizing (H_2S) environments to understand the impact of these treatments on the MoS_2 structural evolution.

Experiment

Atomic Layer Deposition

ALD films were grown in a custom viscous flow tube reactor as reported previously[69]. Molybdenum hexafluoride (MoF_6, Advanced Research Chemicals Inc.) and hydrogen sulfide (H_2S, 99.5%, Sigma Aldrich) were used to grow MoS_2. The delivery pressure for both precursors were controlled using a regulator and a 100 μm orifice. In our reactor configuration, the partial pressure for the MoF_6 was 60 mTorr, while the H_2S was 400 mTorr. Both chemicals are extremely hazardous and great care must be taken when working with them. Vented gas cabinets and cross purge assemblies must be used to ensure safety. Two different substrates were used to carry out the X-ray scattering experiments. For the XAS experiments, aluminum oxide powder (Al_2O_3, Sigma Aldrich) was distributed using a pulsing scheme of 20-90-20-90 sec for 200 cycles to ensure a bulk film was grown. Following this deposition, portions of this powder were loaded on a hot stage, evacuated for > 30 minutes, and then heated to 400 ℃ and 600 ℃ in a H_2 environment for 30 minutes. During annealing the H_2 partial pressure was approximately 2 Torr.

For the PDF measurements, 50 cycles of MoF_6 and H_2S were used to coat OH-terminated carbon nanotubes (CNT-OH, Nanostructured & Amorphous Materials, Inc.) using the same pulsing scheme as described above. Portions of powder from this

deposition were again placed onto a hot stage and annealed at 400 ℃ and 600 ℃ separately in both H_2 and H_2S environments. A 2 Torr H_2 partial pressure was again used, while the H_2S was kept at 1 Torr. CNT-OHs were used for PDF measurements to reduce the background signal introduced by the substrate and thereby limit subtraction artifacts during analysis.

Characterization

XPS was performed on a Thermo Fischer K-Alpha+. The XPS data was analyzed using Thermo Scientific Avantage software, and all spectra were referenced to the C1s peak (284.8 eV). Fitting of the 2p and 3d peaks were constrained according to the spin-orbit split doublet peak areas and FWHM according to the relevant core level using a 30% mixed Gaussian-Lorentzian peak shape. Raman spectroscopy was performed at room temperature on a Renishaw inVia confocal microscope system using an 8mW 633 nm laser and 50x objective with a spot size of ~ 1 μm. The peak positions were calibrated to a Si standard. Powder samples were imaged in a field emission JEOL 2100 transmission electron microscope (TEM) at 200 keV. The powders were dispersed in approximately 2 mL of methanol and sonicated for 20 – 30 seconds. Small amounts of the suspension were dropped onto carbon support grids for imaging.

XAS experiments were carried out at the Advanced Photon Source (APS) at Argonne National Laboratory on beamline 10-BM [109]. Molybdenum foil was referenced, and a MoS_2 bulk powder (< 2 μm, 99%,Sigma Aldrich) was also used to help determine the amplitude reduction factor, S_0^2, parameter [103]. Powder was applied to Kapton tape and placed in the beam path. XAFS fitting was performed using the Demeter suite to view (Athena) and fit structural models (Artemis, and Feff) [110]. HE-XRD

measurements were carried out at the APS using beamline 11-ID-C with a 2048 x 2048 image-plate detector with a sample-to-detector distance of 288 mm and beam energy of 105 keV. PDF analysis was performed using GSAS-II [111]. Center corrections were performed with a NIST standard: CeO_2, SRM674b. Full integration of the images were performed from 0.7 to 32 Q ($Å^{-1}$, where $Q = 4\pi \sin(\theta)/\lambda$), which removed artifacts from the beam stop. The data from blank CNT-OH samples were subtracted to remove any container and substrate effects. FullRMC, a reverse Monte Carlo calculation suite, was used to fit the PDF models to two starting atomic structures [112]. Using built-in packages, an amorphous S-Mo-S "molecule" was distributed in a 50 $Å^3$ cube filling the volume with 1410 molecular units. The second model used the MoS_2 2H structure consisting of 10 layers of MoS_2 (5 unit cells in c direction). Each layer was extended to include 16 unit cells in *a* and *b* crystallographic directions. Periodic boundary conditions were enforced for both models. Bond length distributions were extracted from the atomic models generated by the fullrmc fitting procedure using the I.S.A.A.C.S. software package [113].

Results and Discussion

Fig. 22 shows Raman spectra acquired from the as-deposited MoS_2 coated onto CNT-OH powders using 50 ALD MoS_2 cycles and after annealing treatments at 400°C and 600°C in H_2 and H_2S environments. The as-deposited MoS_2 did not show any of the fundamental peaks for layered MoS_2, indicating that the sample is amorphous. However, the samples annealed at 400 °C in either H_2 and H_2S showed small peaks associated with the in-plane and out-of-plane modes. These peaks grew in magnitude when the samples

were annealed at 600 ℃. These results are consistent with previous reports of MoS_2 ALD using other precursor combinations reported in the literature [44], [57].

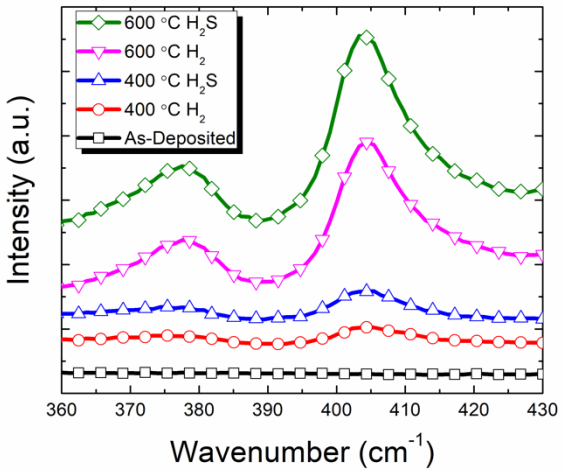

Fig. 22 Raman spectra of as-deposited and annealed films. The as-deposited film lacks the characteristic Raman signals for layered MoS_2, but these signals appear after annealing for 30 min. at 400 ℃ and 600 ℃ in either H_2 or H_2S, indicating crystallization of the films.

Next, the MoS_2 coated CNT-OH were dispersed onto a carbon grid and imaged in a TEM to determine the MoS_2 film thickness and to investigate the morphological changes caused by annealing. Fig. 23 shows TEM images recorded for the as-deposited film (Fig. 23(a)) and after annealing at 400 ℃ (Fig. 23(b)) and 600℃ (Fig. 23(c)) in H_2S. Little to no difference was observed by TEM between the films annealed in H_2 and in H_2S annealing.

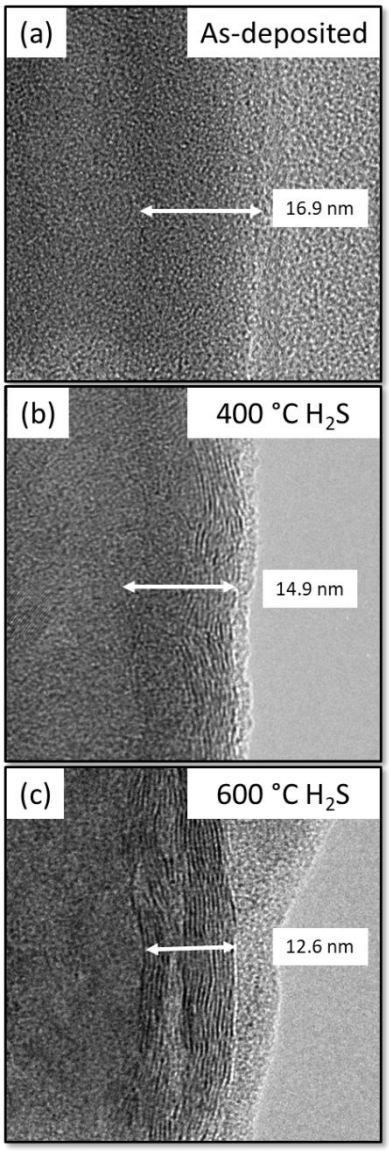

Fig. 23 TEM images of 50 ALD cycles of MoS_2 on CNT-OH: (a) as-deposited, (b) following 400 °C 30 min anneal in H_2S, (c) following 600 °C 30 min anneal in H_2S. The as-deposited films appears amorphous, but a layered structure is observed for the annealed films. Approximatly 20 layers are formed on the CNTs after a 600 °C anneal in H_2S.

The as-deposited films in Fig. 23(a) appear amorphous and conform well to the surface of the CNTs. Using the film thickness measured by TEM in Fig. 23(a), the growth per cycle (GPC) of the as-deposited films was determined to be 3.4 Å/cycle. This is significantly more than our previously estimate of 0.42 Å/cycle based on QCM and ellipsometry measurements of films on planar samples [65]. This discrepancy may result

from insufficient purging of the high surface area carbon powder or from thermal decomposition of the MoF_6 precursor [41]. Samples annealed at 400 ℃ showed a decrease in thickness, measured by TEM, which was expected because of the crystallization of the film. Layered structures appear in the samples annealed at 400 ℃ (Fig. 23(b)), and samples annealed at 600 ℃ (Fig. 23(c)) exhibit clear long-range crystallinity, with a clear interface between the CNT and the MoS_2. Counting the dark intensity regions of the film annealed at 600 ℃, approximately 20 layers were observed with a total thickness of 12.6 nm, which is consistent with a MoS_2 layer thickness of 0.6 nm [114] The TEM results confirm our previous finding that at relatively low annealing temperatures, a layered structure is obtainable using MoF_6 and H_2S [65]. Additionally, we observe gaps between the layers of the MoS_2 films annealed at 600 ℃. These gaps may arise because (1) the films are under stress as-deposited and this stress is relieved upon annealing leading to a separation of the layers or (2) the CNT-OH restructures or pyrolyzes and shrinks away from the MoS_2 during annealing. Thickness variations and voids, described above, made it difficult to establish accurate thickness measurements for the samples annealed at 600 ℃ by TEM.

To further characterize the as-deposited films, XAFS data from the Mo K absorption edge (20 keV) was obtained for 200 cycle MoS_2 films grown on Al_2O_3 powder. Measurements were carried out in fluorescence mode with an energy dispersive Vortex detector with an energy out to 11.8 $Å^{-1}$. Fig. 24 shows XAS spectra for three measured conditions, including a MoS_2 powder reference sample. Qualitatively, little difference is visible between the ALD MoS_2 and the reference indicating similar Mo coordination environments. Our previous report of MoS_2 ALD using MoF_6 and H_2S

found ~16% oxygen in the films, which was thought to arise from reaction with ambient moisture when the samples were removed from the reactor at the 200°C growth temperature [65]. To reduce this effect, we cooled our ALD reactor down to ~40 °C before removing the samples into the air. If the ALD-grown MoS_2 films contained MoO_2 and MoO_3, XAFS data would display signature features of these phases in the X-ray absorption near edge (XANES) region (Fig. 24) [115], [116].

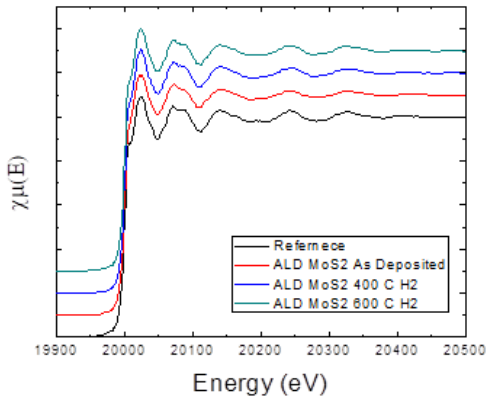

Fig. 24 X-ray absorption spectra of the Mo K edge for as-deposited MoS_2 on alumina powder and for annealed films. The spectrum of a MoS_2 reference powder is included for comparison. The data indicate similar Mo coordination environments for all films.

However, the ALD-grown MoS_2 lacked the pre-edge feature of MoO_3 and lacked white-line features that would indicate MoO_2 [115], [116]. The absence of these features and the agreement with the MoS_2 reference indicate that the films had minimal oxygen content. In contrast to these X-ray measurements of the bulk powder, XPS of the as-deposited films (Fig. 25 and (b)) revealed oxygen peaks consistent with MoO_x species, estimated at 28%. Given the extreme surface sensitivity of the XPS, the oxygen peaks can be attributed primarily to surface oxidation, which would be enhanced on a high surface area powder.

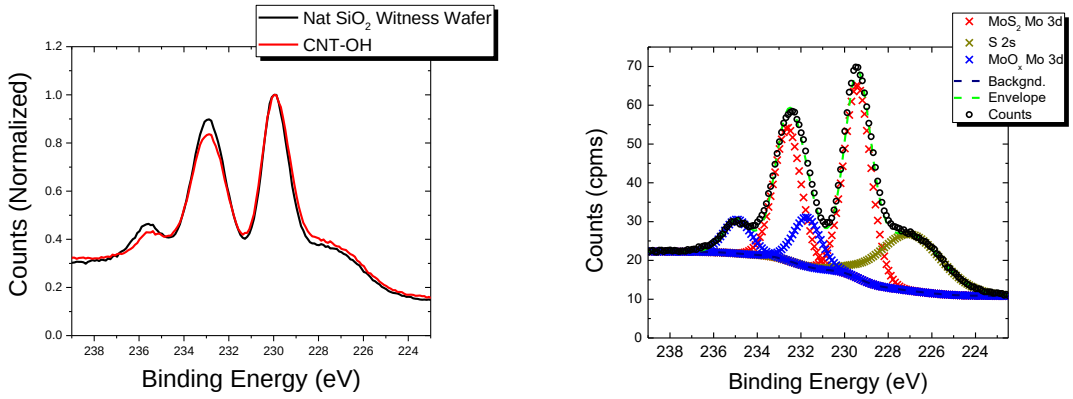

(a) (b)

Fig. 25 XPS scans of the Mo 3d region of the (a) SiO_2 witness wafer and the CNT-OH nanotubes. (b) Is the fitted MoS_2 and MoO_x peaks with the S 2s region.

As outlined in the introduction of this chapter, many of the as-deposited ALD MoS_2 films lack or have very weak 2D Raman peaks. This suggests that the as-deposited ALD films lack a layered structure. The XAS measurements provides information about the atomic coordination spheres smaller than the basal planes of MoS_2 (~ 6 Å). Two features are clearly visible in the scattering intensity (|X(R)|) radial distribution plots, which show the coordination spheres of Mo (Fig. 26(a)) for the as-deposited and annealed films and the MoS_2 powder reference. Theoretical ab initio scattering calculations performed with FEFF, using the MoS_2 2H structure, indicated that the first peak is associated with the Mo-S pair peak (1.4 to 2.3 Å) while the second feature arises from the Mo-Mo pair peak (2.3 to 3.3 Å) [73], [105]. The k-space plots of the scattering amplitudes in Fig. 26(b) show that much of the difference between the different samples occurs in the higher k range, which is where the Mo-Mo contribution is the largest.

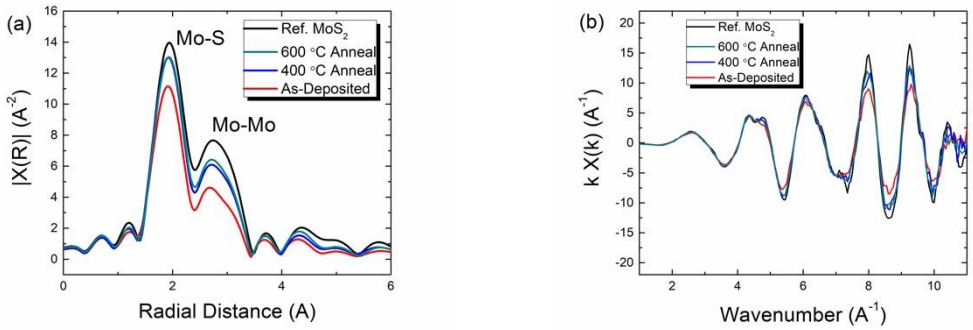

Fig. 26 Analyzed XAS data showing the (a) radial distribution of the scattering intensity around a Mo peak pair and (b) the reciprocal space scattering amplitudes.

Qualitative observations from the XAS data indicate that the Mo-S coordination increases dramatically for the samples annealed at 400 and 600 °C when compared to the as-deposited film, but the difference in coordination between the two annealing conditions is minimal. At higher wavenumbers in Fig. 26(b), we see an increase in peak intensity for the annealed MoS_2 films, which indicates an increase in crystallinity. However, none of the ALD films approach the scattering intensity of the reference, suggesting that the MoS_2 films still contain disorder.

To quantify the atomic structural changes during annealing, the XAFS data were fit using the first two coordination shells of Mo. This fit was carried out using the Artemis software package [110]. Using the bulk MoS_2 and the 2H MoS_2 structure, the amplitude reduction factor, S_0^2, was determined to be 0.8. This factor was used for the as-deposited and annealed samples. Fitting the first two single scattering peaks in Fig. 26(a), which correspond to Mo–S and Mo–Mo, we can start to understand the atomic structural changes during annealing. A summary of the scattering distances is provided in Table 6, and Fig. 27 is a plot of the coordination numbers determined from XAFS modeling for the as-deposited and annealed MoS_2 films.

Table 6 Fitting parameters/results for Artemis structure fitting of MoS_2 films.

	Standard		As dep		400 ℃		600 ℃	
	Mo	S	Mo	S	Mo	S	Mo	S
ΔE_0	2.8(8)	2.8(8)	1.5(7)	1.5(7)	2.3(7)	2.3(7)	2.4(8)	2.4(8)
R	3.18(2)	2.408(5)	3.160(5)	2.405(4)	3.166(6)	2.408(4)	3.170(5)	2.408(5)

The Mo–S coordination numbers of the samples annealed at 400 °C and 600 °C are very similar to the standard, while the Mo–Mo coordination number of the ALD samples is significantly lower than the bulk MoS_2 reference. The Mo coordination was found to be as small as 2.8 for as-deposited ALD MoS_2, and when annealed in H_2, the Mo-Mo coordination number increased to approximately 4.3. This value is still quite low when compared to the theoretical value of six; however, the reference is also lower than this theoretical value. An explanation could be a consequence of the small domain sizes of the samples and scattering contributions from edge defects. Interestingly, in this work only a small increase in the Mo-Mo coordination number was observed when increasing the annealing temperature from 400 to 600 ℃. Because most of the disorder occurs between the Mo-Mo pair peak, the in-plane structure is possibly perturbed. The perturbation is most likely causing the asymmetry in the Raman spectra (Fig. 22), which is similarly found in ion damaged films [117]. Scattering from phonon modes in disordered films also leads to asymmetry in the Raman E_{2g} peaks for ALD films [62].

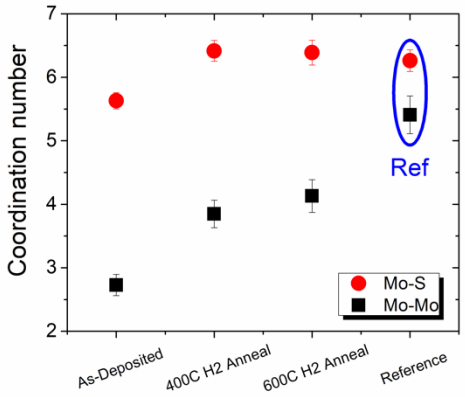

Fig. 27 Coordination numbers of the Mo-S and Mo-Mo single scattering lengths for the as-deposted and annealed MoS_2 films, as well as a bulk MoS_2 reference.

Transmission HE-XRD measurements were performed in an attempt to understand the structures of the ALD film. The sample-detector distance and the beam center were set to maximize the diffraction angle or Q range by calibrating to a NIST CeO_2 powder. In these experiments, hydroxylated carbon nanotubes were used as the growth substrate. Not only do hydroxylated carbon nanotubes have lower atomic number than the alumina powder, but have a small background, which is easily subtracted for data analysis. Because of the increase in surface area, the number of ALD cycles was decreased from 200, as used for the XAS measurements, to 50 total ALD cycles. In these experiments, H_2S was a reducing agent when annealing the powders. Using the GSASII software package, a full integration (360°) was used [111]. The beam stop limited our low Q range to ~0.7 $Å^{-1}$ and integrated out to 32 $Å^{-1}$. Again, GSASII was used to compute pair distribution functions (PDFs) from the diffraction data, Fourier transforms were performed and were optimized for the as-deposited films, and the optimized parameters were used for all other fits. Fig. 28(a) and (b) compare normalized PDFs for the full distance ranges for both the H_2 and H_2S annealing conditions, respectively.

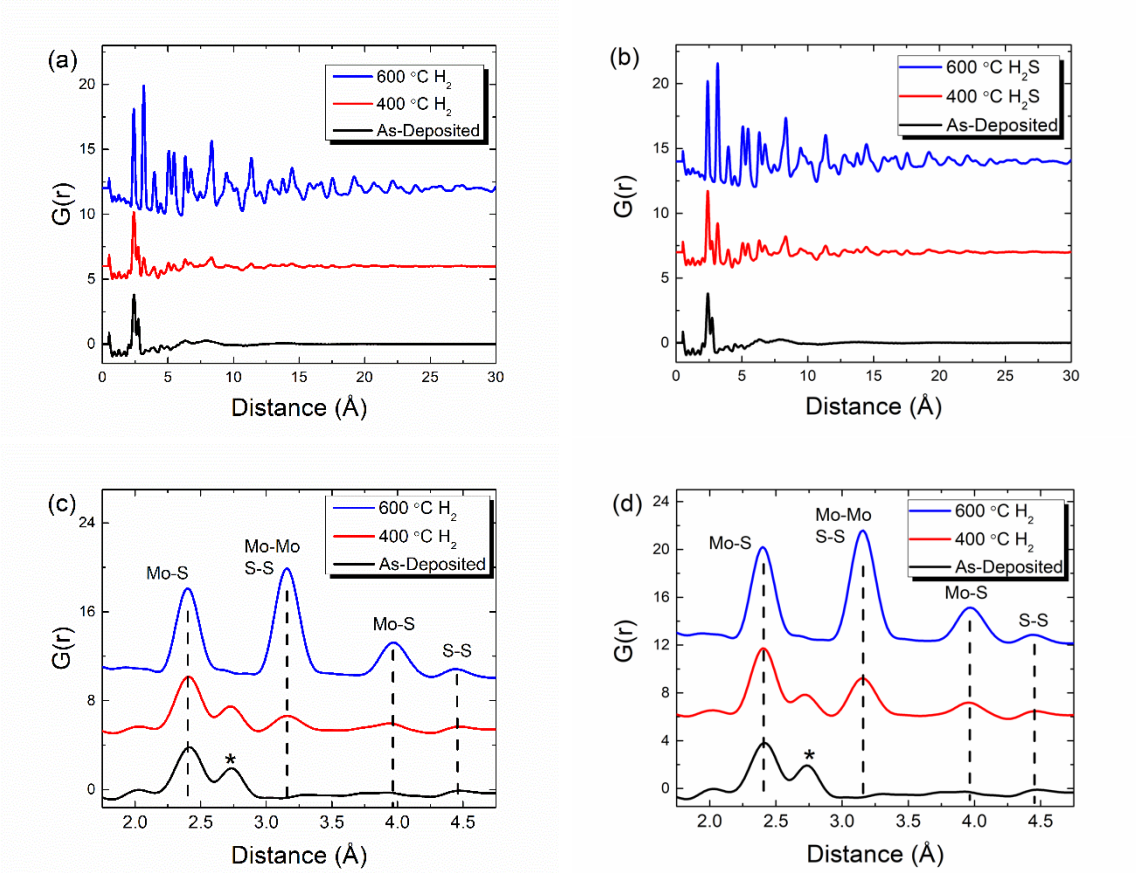

Fig. 28 Normalized pair distributions from HE-XRD of MoS_2 deposited on CNT-OH comparing the as-deposited to annealed conditions in (a) H_2 and (b) H_2S. Zoomed in regions of the first few pair distances of (c) H_2 annealed and (d) H_2S anneal. Dotted lines are from a crystal file from of MoS_2 2H, which was simulated to determine where each contirbution of pair distances occur. Curves are offset vertically forclarity.

PDF measurements of the as-deposited MoS_2 films (Fig. 28(a) and (b)) are essentially featureless at atomic pair distances > 5 Å, and this is consistent with the films being X-ray amorphous [65]. A clear increase in crystallinity is apparent for the 400 °C anneal in both H_2 and H_2S, as features appear at atomic pair distances > 5Å. Sharper features at larger pair distances, for the samples annealed at 600°C in Fig. 28(a) and (b), indicate further crystallization. Fig. 28(c) and (d) show expanded views of the PDF data between 1 and 5 Å, where the scattering bonding pairs associated with the peaks are labeled and dotted lines indicate the ideal positions from a perfect MoS_2 crystal. The as-

deposited films seem to only show Mo-S pair peak as well as an unidentified peak at a pair distance of approximately 2.74 Å. Cramer *et al.* attempted to make amorphous MoS_3 be thermally decomposing ammonium paramolybdate ($(NH_4)_2MoS_4$) and H_2S [118]. XAFS analysis indicated clusters of $[Mo_3S(S_2)_6]^{2-}$ best fit their measurements of the amorphous structure. The peak at 2.74 Å could be explained by the presence of $[Mo_3S(S_2)_6]^{2-}$ ion clusters (Mo-Mo = 2.72) or MoS_3 (Mo-Mo = 2.745) [118], [119]. MoS_3 was proposed to be the thermodynamically stable product from MoF_6/H_2S ALD [65], however a Mo-Mo peak should also appear at 3.158 Å [118]. No peak was observed above 3 Å in the as-deposited ALD film which would suggest that the $[Mo_3S(S_2)_6]^{2-}$ is a more probable structure. The stoichiometry of these ion clusters are identical to MoS_3, however evidence of Mo-Mo bonds account for the reduction of the Mo to a 4^+ state and oxidation of the sulfur [118]. Determining the differences between MoS_2 or MoS_3 using XPS from the Mo 3d peaks is difficult because of their similar binding energies of 229.0 eV and 290.1 eV, respectively [119]. However, two doublets best describe the S 2 p envelope in Fig. 29, and match well previous studies outlining a S^{2-} and S_2^{-2} environment as found in the $[Mo_3S(S_2)_6]^{2-}$ clusters [118], [120].

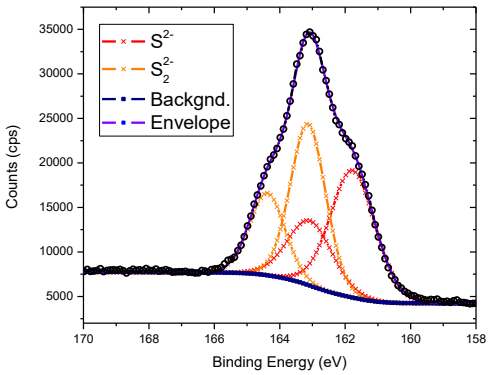

Fig. 29 High resolutions scan of S2p region showing two separate sulfur environments: S^{2-} and S_2.

Moreover, Mo has 7-fold coordination to S in these clusters, which could explain the Mo-S coordination numbers > 6 measured above in the XAS data. Unfortunately, attempts to incorporate this scattering length into the model failed to improve the fit of the XAS data. After annealing at 400 °C, the samples show small peaks that match well with the MoS_2 structure, and a small peak arising from the clusters is still present. At 600 °C, the peak at 2.74 Å, which we attribute to $[Mo_3S(S_2)_6]^{2-}$ clusters, disappears, and a well-formed MoS_2 structure is obtained. However, if the under-coordination of Mo-Mo is an indication of the $[Mo_3S(S_2)_6]^{2-}$ clusters, then the XAS data in Fig. 27 indicates that some clustering is still present following annealing at 600 °C.

Reverse Monte Carlo fitting (fullrmc software [112]) was used to analyze the PDF data in order to better define the ALD MoS_2 structures. Two structures were the input: an amorphous structure, notated as (*a*), made up of 1410 MoS_2 molecular units in a 50 $Å^3$ volume, and a crystalline structure, notated as (*c*), starting with a 2H unit cell, which was expanded into a larger supercell. The amorphous and crystalline structures are depicted in Fig. 30(a) and (b), respectively.

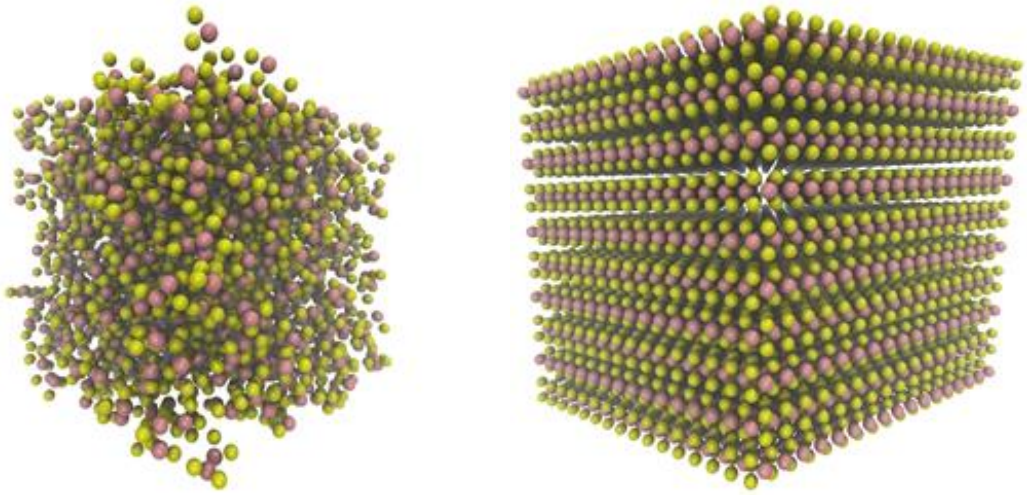

(a) (b)

Fig. 30 Images of the starting models used as input structures for fullrmc for the (a) amorphous and (b) crystalline (2H phase) MoS_2 films. Both super cells fill a 50 $Å^3$ volume. Yellow spheres represent sulfur while the violet spheres are molybdenum.

Using these starting structures, the atomic positions were optimized to fit the experimental PDF data using translations, swaps, and removes. Translations used a step size of 0.1 Å and the number of accepted moves was set to 2.7 x 10^7. Swaps, exchange random Mo and S pairs, while the removes, remove a single atom from the structure. This only allowed 5000 attempts to remove Mo or S. This changed the final stoichiometry minimally as it could adversely affect the chemistry. After minimization the as-deposited structure's Mo:S ratio was 1:1.98, while the 600 ℃ structure was 1:2.05. These small changes indicate that significant the removes had a minimal impact and were not required to fit the PDF data. The coordination numbers, CN, from the model fits were compared to the XAS data as a check of the validity of the models as outlined in Table 7.

Table 7 Fitting parameters and coordination numbers from RMC models of both amorphous and crystalline MoS_2 labeled *a* and *c* respectively.

	As-deposited		400 °C H_2		400 °C H_2S		600 °C H_2		600 °C H_2S	
	a	*c*	*a*	*c*	*a*	*c*	*a*	*c*	*a*	*c*
χ^2	56.48	61.02	52.34	47.57	67.04	48.84	278.13	71.45	247.09	65.99
Mo-Mo CN	1.94	3.46	2.23	3.66	2.11	4.18	1.91	4.82	1.95	4.86
Mo-S CN	2.46	6.00	2.23	5.84	2.25	5.75	2.18	5.08	2.21	5.17

The fit parameter, χ^2, is an indication of the quality of fit, with lower values indicating a better fit. For the as-deposited film, χ^2 is lower for the amorphous structure compared to the crystalline structure, indicating that the amorphous structure better represents the as-deposited MoS_2. In contrast, χ^2 is lower for the crystalline structure compared to the amorphous structure for all the annealed samples, indicating that the crystalline structure better represents the annealed MoS_2. χ^2 increases dramatically for the amorphous structure at 600°C, indicating a very poor fit.

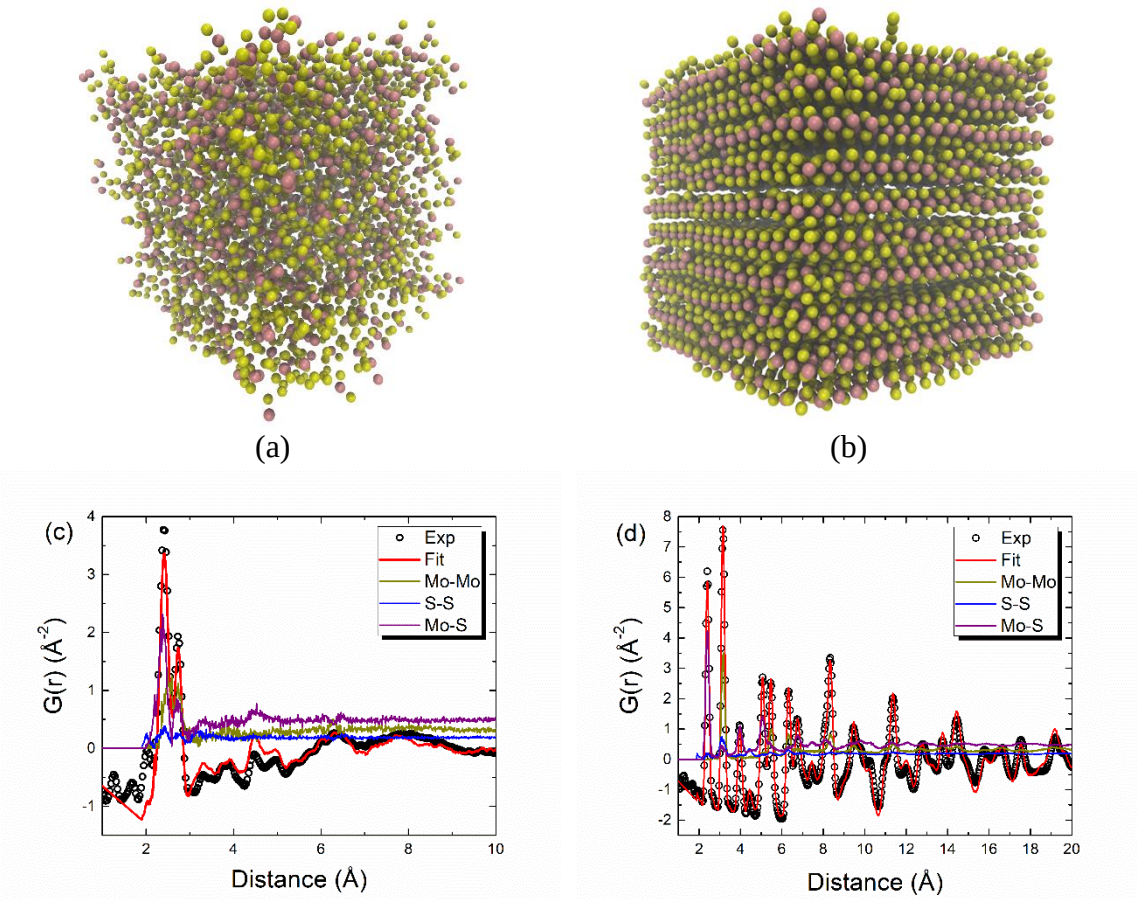

Fig. 31 (a) Shows a image of the simulated as-deposted film starting with an *amorphous* structure while (b) shows the 600 ℃ H_2S annealed model from a *crystalline* initial structure. (c) and (d) are the associated normalized pair distribution functions for the models forcomparions with the data.

The resulting fit and models for the PDF data are shown in Fig. 31. Fig. 31(a) and (b) show the final model structures for the as-deposited and 600 ℃ H_2S films, respectively. Only local variations in the atomic structures were observed when fitting the experimental data for the as-deposited film with the amorphous structure in Fig. 31(a). However, long-range structural coherence can be seen after fitting the experimental data for the annealed film with the periodic structure in Fig. 31(b). Interestingly, the annealed film (Fig. 31(b) and (d)) exhibits a collective movement visible as bending of the layers, which could be an artifact of the ALD growing on the small multi-walled nanotubes or defects in the layers. Both bending and 2D defects are also visible by TEM in Fig. 23(c).

Next, the software package I.S.A.A.C.S. was used to extract bond length distributions from the atomic models derived from the fullrmc fitting procedure in Fig. 32 [113]. This helps visualize the individual atom pair distributions that contribute to the overall signals in the PDF data. For instance, the peak at 3.1 Å in Fig. 28(c) and Fig. 28(d) arises from a combination of Mo-Mo and S-S bond pairs. For the as-deposited films, the minimized amorphous model was used as the input structure, while for all annealed films; the minimized crystalline structure was used. Fig. 32(a) shows the distributions of nearest neighbors for the Mo-Mo pairs. The as-deposited film has a large, broad distribution starting at about 2.3 Å to 2.9 Å; however, molybdenum metal has a pair distance of 2.7 Å, which would suggest that any value below this is nonsensical and a consequence of the fitting procedure. The fullrmc algorithm accepts a percentage of rejected translations/swaps/removes. For the calculations, this value is 30%. Interestingly, by ignoring the data below the 2.7 Å, , the Mo-Mo distances are forced to much lower values matching closely to the $[Mo_3S(S_2)_6]^{2-}$ clusters (~2.8 Å) proposed above with little to no MoS_2 [118].

The as-deposited Mo-S pairs exhibit two distributions, which are attributed to the $[Mo_3S(S_2)_6]^{2-}$ clusters. The values match well with the initial XAFS and proposed models [118], [121]. Fig. 32 (c) shows the S-S distribution and again exhibits two bond distributions for the as-deposited films. In both starting models, a peak is visible around 2.0 Å, which could be caused by either Mo-O bonds or polysulfide bonding, similarly found in elemental sulfur. These sulfide bonds have been proposed in amorphous structures before, but XPS data shows an oxide component (Fig. 25) [118], [121]. Thus,

we attribute the distribution at 2.0 Å to Mo-O bonds formed through oxidation of the films.

From the PDF analysis, we predict a structure that is a mixture of MoS_2 and $[Mo_3S(S_2)_6]^{2-}$. In both species, Mo has a 4^+ oxidation, which argues against the existence of MoS_3. Our previous study of MoS_2 ALD found the films to be sulfur deficient [65], which we suspect to be Mo-Mo bonding, or Mo metal clusters, in the structure. The discrepancy to previous work is most likely caused by the long dose times and high surface area substrate, which could allow the MoF_6 to thermally decompose into Mo metal clusters. This deviation from ideal ALD behavior may allow for control of the composition and stoichiometry of the as-deposited films.

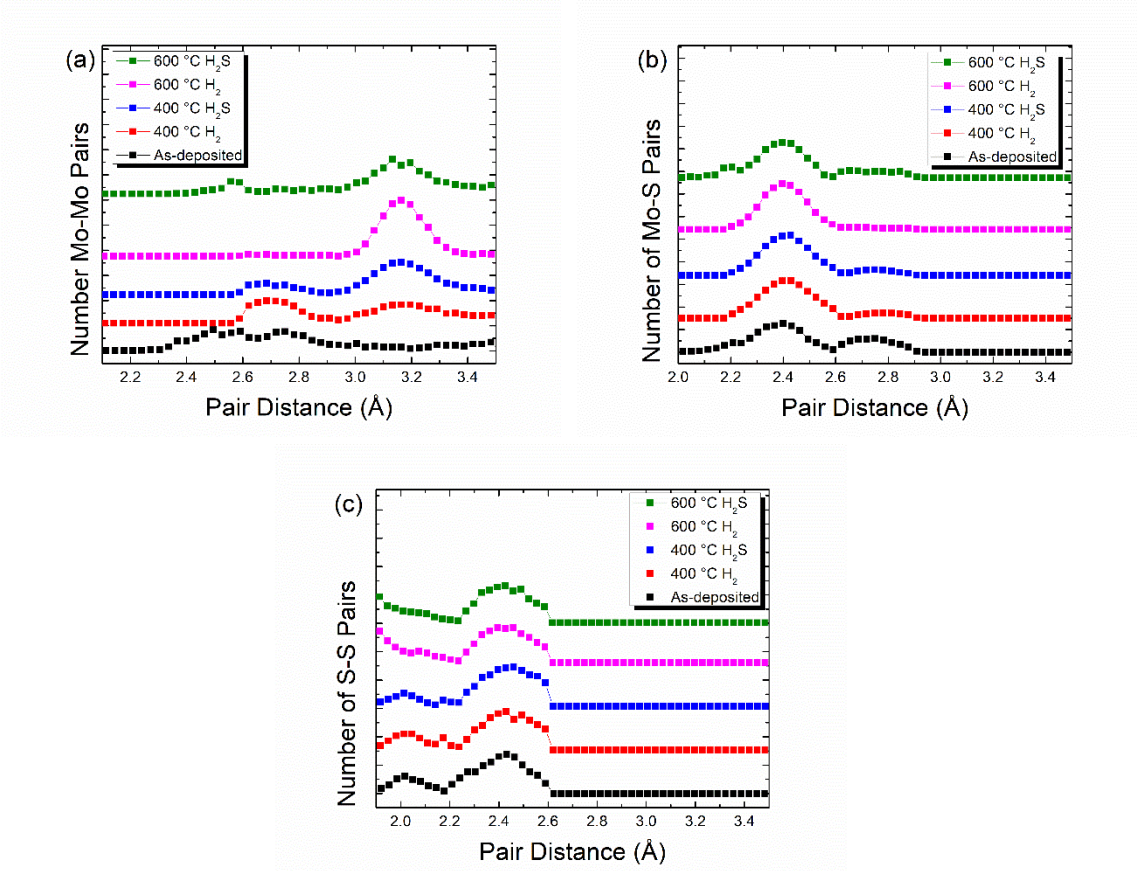

Fig. 32 Bond pair analysis of the minimized structures from fullrmc. The bond length distribution of Mo-Mo (a), Mo-S (b), and S-S (c). For the as-deposited sample, the amorphous structure was used as the starting model, while the crystalline model was used for all of the annealed samples.

Conclusions

ALD MoS_2 was deposited on both Al_2O_3 and CNT-OH powders and analyzed with XAS and HE-XRD measurements. Complementary TEM and Raman measurements demonstrated that the as-deposited were amorphous, but after annealing at 600 °C in H_2 or H_2S, TEM revealed a layered structure, and TEM and Raman indicated a crystalline film. Analyzing the XAFS data, the Mo-S and Mo-Mo coordinations were determined. In the as-deposited films, the Mo-Mo coordination was smaller than theoretical models, while the Mo-S coordination number was larger. PDF analysis confirmed an amorphous structure and indicated the presence of $[Mo_3S(S_2)_6]^{2-}$ clusters. This was confirmed by

XPS and RMC modeling, which indicated sulfur polysulfides forming in the clusters. The clusters are close to a MoS_3 structure, but these findings agree with Mo being in a 4^+ oxidation state, as found in the author's prior work. These cluster structures begin to transform into MoS_2 at 400 ℃ and disappear after annealing to 600 ℃. The author's previous work indicated a sulfur deficient film, contrasting with the results reported here, and this discrepancy can be attributed to precursor stability and by-product interactions in the high surface area substrates used here. Adjusting dose and purge times, a near MoS_2 stoichiometric as-deposited film should be attainable, with crystallization to a layered structure after annealing at relatively low temperatures.

CHAPTER SIX: CONCLUSIONS

Summary

In this work, ALD of MoS_2 was demonstrated using MoF_6 and H_2S. Growth at 200 ℃ on SiO_2 yielded amorphous films, which after annealing at 350 ℃ in H_2 became layered. XPS measurements confirmed that the as-deposited films were MoS_2 but, with an appreciable amount of oxygen. MoO_x species was attributed to removal from the growth chamber at 200 ℃ (the growth temperature). The films grown were quite thick, up to 70 nm, and had a platelet like morphology. Measuring the optical bandgap, we found the films match the literature bulk value of 1.3 eV. We looked at the early nucleation regime of MoF_6 and H_2S on ALD Al_2O_3. Like earlier studies, we found a $MoOF_4$ surface species form but disappear when H_2S is introduced. Approximately 5 to 6 cycles of MoF_6 and H_2S is needed before MoS_2 starts to form. This was confirmed by increases in the FTIR base line caused by free carriers in the semiconductor. We hypothesize that during the nucleation period, $MoOF_4$ species will form until all free oxygen on the surface are consumed. Although XPS confirmed MoS_2, it did little to determine the structure of the as-deposited films. XAS measurements were used to probe the structure of the amorphous film. Fitting XAFS data, we found the films were well coordinated with sulfur, but poorly with neighboring molybdenum atoms. HE-XRD experiments coupled with PDF analysis showed clusters of $[Mo_3S(S_6)_2]^{2-}$ in conjunction with MoS_2. The sulfurs in these clusters form polysulfides, which reduce the Mo from 6+ to 4+ making them indistinguishable from MoS_2 via XPS. To help confirm this, reverse

Monte Carlo calculations were fit to the PDF spectrum starting with both an amorphous and crystalline structure. Bond analysis from the minimized structures showed an S-S distance, which correlated with polysulfides, strengthening the case for these clusters. The clusters decompose after annealing in both H_2 and H_2S, yielding a layered structure, which was confirmed by TEM.

This work has major implications in the advancement of electronic materials. We have shown that understanding the chemistry and surface interaction is crucial when depositing thin films. The goal for much of 2D materials research is to obtain a monolayer or few-layer film. If ALD is used to grow 2D materials in electronics, understanding the as-deposited film in the initial stages of growth is crucial because this will eventually become the layered structure. The varying Mo:S ratios found with this chemistry suggests that a stoichiometric as-deposited MoS_2 film may be achievable with the correct substrate. In my opinion, a more crucial point is decreasing the oxygen interactions. We demonstrated MoF_6 has an affinity to oxygen over sulfur and may require a barrier layer or surface treatment to trap any mobile oxygen species. This should decrease the oxygen content and produce a high quality MoS_2 film.

Outlook on 2D Materials in Electronics

2D materials, like graphene, are still a research topic and have yet to break into commercialization in any major way. Although these materials give many gains over their silicon counter parts, many hurdles must be overcome before they will make it into any consumer or industrial device. Much of the current large-scale growth is still based CVD growth methods and requires high temperatures to obtain high quality films. These

high temperature annealing steps make integration into current Si based chip production difficult.

Simple and low-cost chemistries are crucial for integration into products. While MoF_6 and H_2S are quite low cost and have simple chemistry, interface reactions and substrate dependent growth are significant hurdles to overcome. However, like the work here, if we understand how these interfaces form and the structure of the deposited film, we can design around these hurdles.

REFERENCES

[1] M. M. Waldrop, “The chips are down for Moore’s law,” *Nature*, vol. 530, no. 7589, pp. 144–147, Feb. 2016.

[2] K. S. Novoselov, A. K. Geim, S. V Morozov, D. Jiang, Y. Zhang, S. V Dubonos, I. V Crigorieva, and A. A. Firsov, “Electric Field Effect in Atomically Thin Carbon Films,” *Science (80-.).*, vol. 306, no. 5696, pp. 666–669, 2004.

[3] C. Tan, X. Cao, X.-J. Wu, Q. He, J. Yang, X. Zhang, J. Chen, W. Zhao, S. Han, G.-H. Nam, M. Sindoro, and H. Zhang, “Recent Advances in Ultrathin Two-Dimensional Nanomaterials,” *Chem. Rev.*, p. acs.chemrev.6b00558, 2017.

[4] G. R. Bhimanapati, Z. Lin, V. Meunier, Y. Jung, J. Cha, S. Das, D. Xiao, Y. Son, M. S. Strano, V. R. Cooper, L. Liang, S. G. Louie, E. Ringe, W. Zhou, S. S. Kim, R. R. Naik, B. G. Sumpter, H. Terrones, F. Xia, Y. Wang, J. Zhu, D. Akinwande, N. Alem, J. A. Schuller, R. E. Schaak, M. Terrones, and J. A. Robinson, “Recent Advances in Two-Dimensional Materials beyond Graphene,” *ACS Nano*, vol. 9, no. 12, pp. 11509–11539, Dec. 2015.

[5] K. S. Novoselov, D. Jiang, F. Schedin, T. J. Booth, V. V Khotkevich, S. V Morozov, and A. K. Geim, “Two-dimensional atomic crystals,” *Proc. Natl. Acad. Sci. U. S. A.*, vol. 102, no. 30, pp. 10451–10453, 2005.

[6] X. Li, X. Wang, L. Zhang, S. Lee, and H. Dai, “Chemically Derived, Ultrasmooth Graphene Nanoribbon Semiconductors,” *Science (80-.).*, vol. 319, no. 5867, pp. 1229–1232, Feb. 2008.

[7] Y. Yoon and J. Guo, “Effect of edge roughness in graphene nanoribbon transistors,” *Appl. Phys. Lett.*, vol. 91, no. 7, p. 73103, Aug. 2007.

[8] B. Radisavljevic, A. Radenovic, J. Brivio, V. Giacometti, and A. Kis, “Single-layer MoS_2 transistors,” *Nat. Nanotechnol.*, vol. 6, no. 3, pp. 147–150, Mar. 2011.

[9] L. Ma, D. N. Nath, E. W. Lee, C. H. Lee, M. Yu, A. Arehart, S. Rajan, and Y. Wu, "Epitaxial growth of large area single-crystalline few-layer MoS_2 with high space charge mobility of 192 cm2 V−1 s−1," *Appl. Phys. Lett.*, vol. 105, no. 7, p. 72105, 2014.

[10] J. E. Greene, "Review Article: Tracing the recorded history of thin-film sputter deposition: From the 1800s to 2017," *J. Vac. Sci. Technol. A Vacuum, Surfaces, Film.*, vol. 35, no. 5, p. 05C204, 2017.

[11] C. F. POWELL, J. M. BLOCHER, and J. H. OXLEY, *Vapor Deposition. Edited by Carroll F. Powell, Joseph H. Oxley, John M. Blocher, Jr., Etc. [By Various Authors. With Illustrations.]*. New York, 1966.

[12] H. O. Pierson, *Handbook of Chemical Vapor Deposition: Principles, Technology and Applications*. Elsevier Science, 1999.

[13] J. A. Thornton, "High Rate Thick Film Growth," *Annu. Rev. Mater. Sci.*, vol. 7, no. 1, pp. 239–260, Aug. 1977.

[14] A. C. Jones and M. L. Hitchman, "Overview of Chemical Vapour Deposition," in *Chemical Vapour Deposition: Precursors, Process and Applications*, A. C. Jones and M. L. Hitchman, Eds. Royal Society of Chemistry, 2009.

[15] Q. A. Acton, *Chemical Processes—Advances in Research and Application: 2013 Edition: Scholarly Brief*. ScholarlyEditions, 2013.

[16] Intel, "Intel® 14 nm Technology," 2014. [Online]. Available: http://www.intel.com/content/www/us/en/silicon-innovations/intel-14nm-technology.html.

[17] S. M. George, "Atomic Layer Deposition: An Overview," *Chem. Rev.*, vol. 110, no. 1, pp. 111–131, 2010.

[18] T. Suntola and J. Antson, "US Patent 4058430 (1977)," *Google Sch.*, 1996.

[19] A. A. Malygin, V. E. Drozd, A. A. Malkov, and V. M. Smirnov, "From V. B. Aleskovskii's 'framework' Hypothesis to the Method of Molecular Layering/Atomic Layer Deposition," *Chem. Vap. Depos.*, vol. 21, no. 10–12, pp.

216–240, 2015.

[20] R. L. Puurunen, “Surface chemistry of atomic layer deposition: A case study for the trimethylaluminum/water process,” *J. Appl. Phys.*, vol. 97, no. 12, p. , 2005.

[21] J.-W. Lim, H.-S. Park, and S.-W. Kang, “Kinetic Modeling of Film Growth Rate in Atomic Layer Deposition,” *J. Electrochem. Soc.*, vol. 148, no. 6, p. C403, 2001.

[22] I. M. Association, “Molybdenum mining & processing.” [Online]. Available: http://www.imoa.info/molybdenum/molybdenum-mining-processing.php. [Accessed: 02-Sep-2018].

[23] W. O. Winer, “Molybdenum disulfide as a lubricant: A review of the fundamental knowledge,” *Wear*, vol. 10, no. 6, pp. 422–452, Nov. 1967.

[24] F. Lévy, *Crystallography and Crystal Chemistry of Materials with Layered Structures*, no. 2. Dordrecht, Holland ; Boston: Springer Netherlands, 1976.

[25] V. Alexiev, R. Prins, and T. Weber, “Ab initio study of MoS_2 and Li adsorbed on the (10$\bar{1}$0) face of MoS_2,” *Phys. Chem. Chem. Phys.*, vol. 2, no. 8, pp. 1815–1827, 2000.

[26] F. Wypych and R. Schöllhorn, “1T-MoS_2, a new metallic modification of molybdenum disulfide,” *J. Chem. Soc., Chem. Commun.*, no. 19, pp. 1386–1388, 1992.

[27] T. Heine, “Transition Metal Chalcogenides: Ultrathin Inorganic Materials with Tunable Electronic Properties,” *Acc. Chem. Res.*, vol. 48, no. 1, pp. 65–72, 2015.

[28] Q. H. Wang, K. Kalantar-Zadeh, A. Kis, J. N. Coleman, and M. S. Strano, “Electronics and optoelectronics of two-dimensional transition metal dichalcogenides,” *Nat. Nanotechnol.*, vol. 7, no. 11, pp. 699–712, Nov. 2012.

[29] K. Zhang, S. Hu, Y. Zhang, T. Zhang, X. Zhou, Y. Sun, T.-X. Li, H. J. Fan, G. Shen, X. Chen, and N. Dai, “Self-Induced Uniaxial Strain in MoS_2 monolayers with local van der Waals-stacking interlayer interactions,” *ACS Nano*, vol. 9, no. 3, pp. 2704–2710, 2015.

[30] H. Huang, Y. Cui, Q. Li, C. Dun, W. Zhou, W. Huang, L. Chen, C. A. Hewitt, and

D. L. Carroll, “Metallic 1T phase MoS_2 nanosheets for high-performance thermoelectric energy harvesting,” *Nano Energy*, vol. 26, pp. 172–179, 2016.

[31] M. Chhowalla, H. S. Shin, G. Eda, L.-J. Li, K. P. Loh, and H. Zhang, “The chemistry of two-dimensional layered transition metal dichalcogenide nanosheets.,” *Nat. Chem.*, vol. 5, no. 4, pp. 263–75, Apr. 2013.

[32] O. Ruff and E. Ascher, “Einige physikalische Konstanten von SiF_4, WF_6 und MoF_6,” *Zeitschrift für Anorg. und Allg. Chemie*, vol. 196, no. 1, pp. 413–420, 1931.

[33] D. W. Osborne, F. Schreiner, J. G. Malm, H. Selig, and L. Rochester, “Heat Capacity and Other Thermodynamic Properties of MoF_6 between 4° and 350 °K,” *J. Chem. Phys.*, vol. 44, no. 7, pp. 2802–2809, 1966.

[34] N. Lifshitz, D. S. Williams, C. D. Capio, and J. M. Brown, “Selective molybdenum deposition by LPCVD,” *J. Electrochem. Soc.*, vol. 134, no. 8, pp. 2061–2067, 1987.

[35] W. Y. Lee, T. M. Besmann, and M. W. Stott, “Preparation of MoS_2 Thin Films By Chemical Vapor Deposition,” *J. Mater. Res.*, vol. 9, no. 6, pp. 1474–1483, 1994.

[36] W. Y. Lee and K. L. More, “Crystal orientation and near-interface structure of chemically vapor deposited MoS_2 films,” *J. Mater. Res.*, vol. 10, no. 1, pp. 49–53, 1995.

[37] E. Orij N., M. de Croon H.J.M., and G. Marin B., “Modelling of the Deposition of Molybdenum on Silicon from Molybdenum Hexafluoride and Hydrogen,” *J. Phys. IV Fr.*, vol. 5, no. C5, pp. C5-331-C5-338, 1995.

[38] T. Sahin, E. J. Flanigan, and J. T. Sears, “Low Pressure Chemical Vapour Deposition of Molybdenum: 1. Kinetics and Reaction Mechanisims,” in *Tungsten and Other Refractory Metals for VLSI Applications II*, 1986, vol. 1, pp. 199–205.

[39] T. Sahin and C.-S. Park, “Low Pressure Chemical Vapor Deposition of Molybdenum By Silicon Reduction of MoF6,” in *Tungsten and Other Refractory Metals fo VLSI Applications IV*\, 1988, pp. 253–256.

[40] J. S. Gama, J. B. Wagener, and P. L. Crouse, “A thermogravimetric study of the reactions of molybdenum disilicide with anhydrous hydrogen fluoride and fluorine,” *J. Fluor. Chem.*, vol. 145, pp. 66–69, Jan. 2013.

[41] D. Seghete, G. B. Rayner, A. S. Cavanagh, V. R. Anderson, and S. M. George, “Molybdenum Atomic Layer Deposition Using MoF_6 and Si_2H_6 as the Reactants,” *Chem. Mater.*, vol. 23, no. 7, pp. 1668–1678, Apr. 2011.

[42] S. E. Schulz, B. Hintze, T. Gessner, H. Wolf, and W. Gruenewald, “Selective tungsten CVD on sputtered tungsten for via fill,” *Appl. Surf. Sci.*, vol. 73, no. C, pp. 42–50, 1993.

[43] A. J. M. Mackus, A. A. Bol, and W. M. M. Kessels, “The use of atomic layer deposition in advanced nanopatterning,” *Nanoscale*, vol. 6, no. 19, pp. 10941–10960, 2014.

[44] L. K. Tan, B. Liu, J. H. Teng, S. Guo, H. Y. Low, and K. P. Loh, “Atomic layer deposition of a MoS_2 film,” *Nanoscale*, vol. 6, no. 18, pp. 10584–10588, 2014.

[45] L. Liu, Y. Huang, J. Sha, and Y. Chen, “Layer-controlled precise fabrication of ultrathin MoS_2 films by atomic layer deposition,” *Nanotechnology*, vol. 28, no. 19, p. 195605, 2017.

[46] R. Browning, P. Padigi, R. Solanki, D. J. Tweet, P. Schuele, and D. Evans, “Atomic layer deposition of MoS_2 thin films,” *Mater. Res. Express*, vol. 2, no. 3, p. 35006, 2015.

[47] T. A. Ho, C. Bae, S. Lee, M. Kim, J. M. Montero-Moreno, J. H. Park, and H. Shin, “Edge-On MoS_2 Thin Films by Atomic Layer Deposition for Understanding the Interplay between the Active Area and Hydrogen Evolution Reaction,” *Chem. Mater.*, vol. 29, no. 17, pp. 7604–7614, Sep. 2017.

[48] Y. Huang, L. Liu, W. Zhao, and Y. Chen, “Preparation and characterization of molybdenum disulfide films obtained by one-step atomic layer deposition method,” *Thin Solid Films*, vol. 624, pp. 101–105, Feb. 2017.

[49] M. B. Sreedhara, S. Gope, B. Vishal, R. Datta, A. J. Bhattacharyya, and C. N. R. Rao, “Atomic layer deposition of crystalline epitaxial MoS_2 nanowall networks

exhibiting superior performance in thin-film rechargeable Na-ion batteries," *J. Mater. Chem. A*, vol. 6, no. 5, pp. 2302–2310, 2018.

[50] Y. Jang, S. Yeo, H.-B.-R. Lee, H. Kim, and S.-H. Kim, "Wafer-scale, conformal and direct growth of MoS_2 thin films by atomic layer deposition," *Appl. Surf. Sci.*, vol. 365, pp. 160–165, Mar. 2016.

[51] D. K. Nandi, S. Sahoo, S. Sinha, S. Yeo, H. Kim, R. N. Bulakhe, J. Heo, J. J. Shim, and S. H. Kim, "Highly Uniform Atomic Layer-Deposited MoS_2@3D-Ni-Foam: A Novel Approach to Prepare an Electrode for Supercapacitors," *ACS Appl. Mater. Interfaces*, vol. 9, no. 46, pp. 40252–40264, 2017.

[52] D. Xiong, Q. Zhang, W. Li, J. Li, X. Fu, M. F. Cerqueira, P. Alpuim, and L. Liu, "Atomic-layer-deposited ultrafine MoS_2 nanocrystals on cobalt foam for efficient and stable electrochemical oxygen evolution," *Nanoscale*, vol. 9, no. 8, pp. 2711–2717, 2017.

[53] D. K. Nandi, U. K. Sen, D. Choudhury, S. Mitra, and S. K. Sarkar, "Atomic Layer Deposited MoS_2 as a Carbon and Binder Free Anode in Li-ion Battery," *Electrochim. Acta*, vol. 146, pp. 706–713, Nov. 2014.

[54] J. J. Pyeon, S. H. Kim, D. S. Jeong, S.-H. Baek, C.-Y. Kang, J.-S. Kim, and S. K. Kim, "Wafer-scale growth of MoS_2 thin films by atomic layer deposition," *Nanoscale*, vol. 8, no. 20, pp. 10792–10798, 2016.

[55] A. Valdivia, D. J. Tweet, and J. F. Conley, "Atomic layer deposition of two dimensional MoS_2 on 150 mm substrates," *J. Vac. Sci. Technol. A*, vol. 34, no. 2, 2016.

[56] S. Oh, J. B. Kim, J. T. Song, J. Oh, and S.-H. Kim, "Atomic layer deposited molybdenum disulfide on Si photocathodes for highly efficient photoelectrochemical water reduction reaction," *J. Mater. Chem. A*, vol. 5, no. 7, pp. 3304–3310, 2017.

[57] Z. Jin, S. Shin, D. H. Kwon, S.-J. Han, and Y.-S. Min, "Novel chemical route for atomic layer deposition of MoS_2 thin film on SiO_2/Si substrate.," *Nanoscale*, vol. 6, no. 23, pp. 14453–8, 2014.

[58] T. Zhang, Y. Wang, J. Xu, L. Chen, H. Zhu, Q. Sun, S. Ding, D. Wei, and D. W. Zhang, “High performance few-layer MoS_2 transistor arrays with wafer level homogeneity integrated by atomic layer deposition,” *2D Mater.*, vol. 5, no. 1, p. 15028, Dec. 2017.

[59] X. Li, M. Puttaswamy, Z. Wang, T. C. Kei, A. C. Grimsdale, N. P. Kherani, and A. I. Y. Tok, “A Pressure Tuned Stop-flow Atomic Layer Deposition Process for MoS_2 on High Porous Nanostructure and Fabrication of TiO_2/MoS_2 Core/shell Inverse Opal Structure,” *Appl. Surf. Sci.*, vol. 422, pp. 536–543, Jun. 2017.

[60] S. Shin, Z. Jin, D. H. Kwon, R. Bose, and Y.-S. Min, “High Turnover Frequency of Hydrogen Evolution Reaction on Amorphous MoS_2 Thin Film Directly Grown by Atomic Layer Deposition,” *Langmuir*, vol. 31, no. 3, pp. 1196–1202, 2015.

[61] W. Jeon, Y. Cho, S. Jo, J.-H. Ahn, and S.-J. Jeong, “Wafer-Scale Synthesis of Reliable High-Mobility Molybdenum Disulfide Thin Films via Inhibitor-Utilizing Atomic Layer Deposition,” *Adv. Mater.*, vol. 1703031, p. 1703031, 2017.

[62] T. Jurca, M. J. Moody, A. Henning, J. D. Emery, B. Wang, J. M. Tan, T. L. Lohr, L. J. Lauhon, and T. J. Marks, “Low-Temperature Atomic Layer Deposition of MoS_2 Films,” *Angew. Chemie Int. Ed.*, vol. 56, no. 18, pp. 4991–4995, Apr. 2017.

[63] S. Cadot, O. Renault, M. Frégnaux, D. Rouchon, E. Nolot, K. Szeto, C. Thieuleux, L. Veyre, H. Okuno, F. Martin, and E. A. Quadrelli, “A novel 2-step ALD route to ultra-thin MoS_2 films on SiO_2 through a surface organometallic intermediate,” *Nanoscale*, vol. 9, no. 2, pp. 538–546, 2017.

[64] M. Mattinen, T. Hatanpää, T. Sarnet, K. Mizohata, K. Meinander, P. J. King, L. Khriachtchev, J. Räisänen, M. Ritala, and M. Leskelä, “Atomic Layer Deposition of Crystalline MoS_2 Thin Films: New Molybdenum Precursor for Low-Temperature Film Growth,” *Adv. Mater. Interfaces*, vol. 1700123, p. 1700123, 2017.

[65] A. U. Mane, S. Letourneau, D. J. Mandia, J. Liu, J. A. Libera, Y. Lei, Q. Peng, E. Graugnard, and J. W. Elam, “Atomic layer deposition of molybdenum disulfide films using MoF_6 and H_2S,” *J. Vac. Sci. Technol. A Vacuum, Surfaces, Film.*, vol.

36, no. 1, p. 01A125, Jan. 2018.

[66] S. Letourneau, M. Young, N. Bedford, Y. Ren, A. Yanguas-Gil, A. U. Mane, J. W. Elam, and E. Graugnard, “Synchrotron X-ray structural characterization of molybdenum disulfide prepared by atomic layer deposition,” *Submitted*, 2018.

[67] E.-L. Lakomaa, S. Haukka, and T. Suntola, “Atomic layer growth of TiO_2 on silica,” *Appl. Surf. Sci.*, vol. 60–61, pp. 742–748, Jan. 1992.

[68] N. Lifshitz, J. M. Brown, and D. Williams, “Microstructural Characterization of Molybdenum Flims Deposited by LPCVD,” in *Tungsten and Other Refractory Metals fo VLSI Applications II*, 1986, pp. 215–223.

[69] J. W. Elam, M. D. Groner, and S. M. George, “Viscous flow reactor with quartz crystal microbalance for thin film growth by atomic layer deposition,” *Rev. Sci. Instrum.*, vol. 73, no. 8, pp. 2981–2987, 2002.

[70] H. Li, Q. Zhang, C. C. R. Yap, B. K. Tay, T. H. T. Edwin, A. Olivier, and D. Baillargeat, “From bulk to monolayer MoS_2: Evolution of Raman scattering,” *Adv. Funct. Mater.*, vol. 22, no. 7, pp. 1385–1390, 2012.

[71] O. Research, “HSC Chemistry.” Pori, Finland.

[72] W. A. West and A. W. C. Menzies, “The Vapor Pressures of Sulphur between 100° and 550° with related Thermal Data,” *J. Phys. Chem.*, vol. 33, no. 12, pp. 1880–1892, Jan. 1928.

[73] K. D. Bronsema, J. L. De Boer, and F. Jellinek, “On the structure of molybdenum diselenide and disulfide,” *Zeitschrift für Anorg. und Allg. Chemie*, vol. 540, no. 9–10, pp. 15–17, Sep. 1986.

[74] P. Kumar, M. Singh, R. K. Sharma, and G. B. Reddy, “Reaction mechanism of core–shell MoO_2/MoS_2 nanoflakes via plasma-assisted sulfurization of MoO_3,” *Mater. Res. Express*, vol. 3, no. 5, p. 55021, May 2016.

[75] B. H. Kim, H. H. Gu, and Y. J. Yoon, “Atomic rearrangement of a sputtered MoS2 film from amorphous to a 2D layered structure by electron beam irradiation,” *Sci. Rep.*, vol. 7, no. 1, p. 3874, Dec. 2017.

[76] J. Tauc and A. Menth, “States in the gap,” *J. Non. Cryst. Solids*, vol. 8–10, no. C, pp. 569–585, 1972.

[77] J. Tauc, “Optical Properties of Amorphous Semiconductors,” in *Amorphous and Liquid Semiconductors*, J. Tauc, Ed. Boston, MA: Springer US, 1974, pp. 159–220.

[78] E. A. Davis and N. F. Mott, “Conduction in non-crystalline systems V. Conductivity, optical absorption and photoconductivity in amorphous semiconductors,” *Philos. Mag.*, vol. 22, no. 179, pp. 903–922, 1970.

[79] K. F. Mak, C. Lee, J. Hone, J. Shan, and T. F. Heinz, “Atomically thin MoS2: A new direct-gap semiconductor,” *Phys. Rev. Lett.*, vol. 105, no. 13, pp. 2–5, 2010.

[80] A. Tarasov, P. M. Campbell, M.-Y. Tsai, Z. R. Hesabi, J. Feirer, S. Graham, W. J. Ready, and E. M. Vogel, “Highly Uniform Trilayer Molybdenum Disulfide for Wafer-Scale Device Fabrication,” *Adv. Funct. Mater.*, vol. 24, no. 40, pp. 6389–6400, 2014.

[81] J. Jeon, S. K. Jang, S. M. Jeon, G. Yoo, Y. H. Jang, J.-H. Park, and S. Lee, “Layer-controlled CVD growth of large-area two-dimensional MoS 2 films,” *Nanoscale*, vol. 7, no. 5, pp. 1688–1695, 2015.

[82] P. Yang, X. Zou, Z. Zhang, M. Hong, J. Shi, S. Chen, J. Shu, L. Zhao, S. Jiang, X. Zhou, Y. Huan, C. Xie, P. Gao, Q. Chen, Q. Zhang, Z. Liu, and Y. Zhang, “Batch production of 6-inch uniform monolayer molybdenum disulfide catalyzed by sodium in glass,” *Nat. Commun.*, vol. 9, no. 1, p. 979, Dec. 2018.

[83] D. Kahng, “Kahng, Dawon,” 3102230A, 1963.

[84] W. Bao, X. Cai, D. Kim, K. Sridhara, and M. S. Fuhrer, “High mobility ambipolar MoS_2 field-effect transistors: Substrate and dielectric effects,” *Appl. Phys. Lett.*, vol. 102, no. 4, 2013.

[85] Y.-C. Lin, B. Jariwala, B. M. Bersch, K. Xu, Y. Nie, B. Wang, S. M. Eichfeld, X. Zhang, T. H. Choudhury, Y. Pan, R. Addou, C. M. Smyth, J. Li, K. Zhang, M. A. Haque, S. Fölsch, R. M. Feenstra, R. M. Wallace, K. Cho, S. K. Fullerton-Shirey, J. M. Redwing, and J. A. Robinson, “Realizing Large-Scale, Electronic-Grade

Two-Dimensional Semiconductors," *ACS Nano*, vol. 12, no. 2, pp. 965–975, Feb. 2018.

[86] Y. Liu, H. Wu, H.-C. Cheng, S. Yang, E. Zhu, Q. He, M. Ding, D. Li, J. Guo, N. O. Weiss, Y. Huang, and X. Duan, "Toward Barrier Free Contact to Molybdenum Disulfide Using Graphene Electrodes," *Nano Lett.*, vol. 15, no. 5, pp. 3030–3034, 2015.

[87] S. Das, H.-Y. Chen, A. V. Penumatcha, and J. Appenzeller, "High Performance Multilayer MoS_2 Transistors with Scandium Contacts," *Nano Lett.*, p. 121219091726009, 2012.

[88] J. D. Ferguson, A. W. Weimer, and S. M. George, "Atomic layer deposition of ultrathin and conformal Al_2O_3 films on BN particles," *Thin Solid Films*, vol. 371, no. 1, pp. 95–104, 2000.

[89] A. C. Dillon, M. B. Robinson, M. Y. Han, and S. M. George, "Diethylsilane Decomposition on Silicon Surfaces Studied Using Transmission FTIR Spectroscopy," *J. Electrochem. Soc.*, vol. 139, no. 2, pp. 537–543, 1992.

[90] A. Yanguas-Gil, J. A. Libera, and J. W. Elam, "In Situ FTIR Characterization of Growth Inhibition in Atomic Layer Deposition Using Reversible Surface Functionalization," *ECS Trans.*, vol. 50, no. 13, pp. 43–51, Mar. 2013.

[91] A. Yanguas-Gil, J. A. Libera, and J. W. Elam, "Modulation of the growth per cycle in atomic layer deposition using reversible surface functionalization," *Chem. Mater.*, vol. 25, p. 4849, 2013.

[92] G. Sauerbrey, "Verwendung von Schwingquarzen zur Wägung dünner Schichten und zur Mikrowägung," *Zeitschrift für Phys.*, vol. 155, no. 2, pp. 206–222, Apr. 1959.

[93] C. E. Nelson, J. W. Elam, M. A. Cameron, M. A. Tolbert, and S. M. George, "Desorption of H_2O from a hydroxylated single-crystal α-Al_2O_3(0001) surface," *Surf. Sci.*, vol. 416, no. 3, pp. 341–353, Oct. 1998.

[94] A. Rahtu, T. Alaranta, and M. Ritala, "In Situ Quartz Crystal Microbalance and Quadrupole Mass Spectrometry Studies of Atomic Layer Deposition of Aluminum

Oxide from Trimethylaluminum and Water," *Langmuir*, vol. 17, no. 21, pp. 6506–6509, 2001.

[95] Y. Lee and S. M. George, "Atomic Layer Etching of Al_2O_3 Using Sequential, Self-Limiting Thermal Reactions with $Sn(acac)_2$ and Hydrogen Fluoride," *ACS Nano*, vol. 9, no. 2, pp. 2061–2070, 2015.

[96] L. E. Alexander, I. R. Beattie, A. Bukovszky, P. J. Jones, C. J. Marsden, and G. J. Van Schalkwyk, "Vapour density and vibrational spectra of $MoOF_4$ and WOF_4. The structure of crystalline WOF_4," *J. Chem. Soc. Dalt. Trans.*, no. 1, p. 81, 1974.

[97] U. Gross, S. Rüdiger, E. Kemnitz, K.-W. Brzezinka, S. Mukhopadhyay, C. Bailey, A. Wander, and N. Harrison, "Vibrational Analysis Study of Aluminum Trifluoride Phases," *J. Phys. Chem. A*, vol. 111, no. 26, pp. 5813–5819, Jul. 2007.

[98] A. Snelson, "Infrared Spectrum of LiF, Li_2F_2 , and Li_3F_3 by Matrix Isolation," *J. Chem. Phys.*, vol. 46, no. 9, pp. 3652–3656, 1967.

[99] J. W. Elam, A. U. Maine, J. A. Libera, J. N. Hryn, O. H. W. Siegmund, J. McPhate, M. J. Wetstein, A. Elagin, M. J. Minot, A. O'Mahony, R. G. Wagner, W. M. Tong, A. D. Brodie, M. A. McCord, and C. F. Bevis, "Synthesis, Characterization, and Application of Tunable Resistance Coatings Prepared by Atomic Layer Deposition," *ECS Trans.*, vol. 58, no. 10, pp. 249–261, 2013.

[100] C. H. Chang and S. S. Chan, "Infrared and Raman studies of amorphous MoS_3 and poorly crystalline MoS_2," *J. Catal.*, vol. 72, no. 1, pp. 139–148, 1981.

[101] L. Benoist, D. Gonbeau, G. Pfister-Guillouzo, E. Schmidt, G. Meunier, and A. Levasseur, "X-ray photoelectron spectroscopy characterization of amorphous molybdenum oxysulfide thin films," *Thin Solid Films*, vol. 258, no. 1–2, pp. 110–114, Mar. 1995.

[102] P. Lee and G. Beni, "New method for the calculation of atomic phase shifts: Application to extended x-ray absorption fine structure (EXAFS) in molecules and crystals," *Phys. Rev. B*, vol. 15, no. 6, pp. 2862–2883, 1977.

[103] S. Calvin, *XAFS for Everyone*. Boca Raton, FL: CRC/Taylor & Francis, 2013.

[104] Matthew Newville, *Fundamentals of XAFS*. Chicago, IL: Consortium of Advanced Radiation Sources, 2004.

[105] J. J. Rehr, J. J. Kas, F. D. Vila, M. P. Prange, and K. Jorissen, "Parameter-free calculations of X-ray spectra with FEFF9," *Phys. Chem. Chem. Phys.*, vol. 12, no. 21, p. 5503, Jun. 2010.

[106] T. Proffen, S. J. L. Billinge, T. Egami, and D. Louca, "Structural analysis of complex materials using the atomic pair distribution function — a practical guide," *Zeitschrift für Krist. - Cryst. Mater.*, vol. 218, no. 2, p. 132, Jan. 2003.

[107] S. J. L. Billinge and M. G. Kanatzidis, "Beyond crystallography: the study of disorder, nanocrystallinity and crystallographically challenged materials with pair distribution functions," *Chem. Commun.*, no. 7, p. 749, 2004.

[108] V. Petkov, "Nanostructure by high-energy X-ray diffraction," *Mater. Today*, vol. 11, no. 11, pp. 28–38, Nov. 2008.

[109] A. J. Kropf, J. Katsoudas, S. Chattopadhyay, T. Shibata, E. A. Lang, V. N. Zyryanov, B. Ravel, K. McIvor, K. M. Kemner, K. G. Scheckel, S. R. Bare, J. Terry, S. D. Kelly, B. A. Bunker, C. U. Segre, R. Garrett, I. Gentle, K. Nugent, and S. Wilkins, "The New MRCAT (Sector 10) Bending Magnet Beamline at the Advanced Photon Source," in *AIP Conference Proceedings*, 2010, vol. 1234, no. 1, pp. 299–302.

[110] B. Ravel and M. Newville, "ATHENA , ARTEMIS , HEPHAESTUS : data analysis for X-ray absorption spectroscopy using IFEFFIT," *J. Synchrotron Radiat.*, vol. 12, no. 4, pp. 537–541, Jul. 2005.

[111] B. H. Toby and R. B. Von Dreele, "GSAS-II : the genesis of a modern open-source all purpose crystallography software package," *J. Appl. Crystallogr.*, vol. 46, no. 2, pp. 544–549, Apr. 2013.

[112] B. Aoun, "Fullrmc, a rigid body reverse monte carlo modeling package enabled with machine learning and artificial intelligence," *J. Comput. Chem.*, vol. 37, no. 12, pp. 1102–1111, May 2016.

[113] S. Le Roux and V. Petkov, "ISAACS – interactive structure analysis of amorphous

and crystalline systems," *J. Appl. Crystallogr.*, vol. 43, no. 1, pp. 181–185, Feb. 2010.

[114] P. Joensen, R. F. Frindt, and S. R. Morrison, "Single-layer MoS_2," *Mater. Res. Bull.*, vol. 21, no. 4, pp. 457–461, 1986.

[115] T. Ressler, "Bulk Structural Investigation of the Reduction of MoO_3 with Propene and the Oxidation of MoO_2 with Oxygen," *J. Catal.*, vol. 210, no. 1, pp. 67–83, 2002.

[116] B. Lassalle-Kaiser, D. Merki, H. Vrubel, S. Gul, V. K. Yachandra, X. Hu, and J. Yano, "Evidence from in Situ X-ray Absorption Spectroscopy for the Involvement of Terminal Disulfide in the Reduction of Protons by an Amorphous Molybdenum Sulfide Electrocatalyst," *J. Am. Chem. Soc.*, vol. 137, no. 1, pp. 314–321, Jan. 2015.

[117] S. Mignuzzi, A. J. Pollard, N. Bonini, B. Brennan, I. S. Gilmore, M. A. Pimenta, D. Richards, and D. Roy, "Effect of disorder on Raman scattering of single-layer MoS_2," *Phys. Rev. B*, vol. 91, no. 19, p. 195411, May 2015.

[118] S. P. Cramer, K. S. Liang, A. J. Jacobson, C. H. Chang, and R. R. Chianelli, "EXAFS Studies of Amorphous Molybdenum and Tungsten Trisulfides and Triselenides," *Inorg. Chem.*, vol. 23, no. 9, pp. 1215–1221, 1984.

[119] T. Weber, J. C. Muijsers, and J. W. Niemantsverdriet, "Structure of Amorphous MoS_3," *J. Phys. Chem.*, vol. 99, no. 22, pp. 9194–9200, Jun. 1995.

[120] M. De Boer, A. J. Van Dillen, D. C. Koningsberger, and J. W. Geus, "The Structure of Highly Dispersed SiO_2-Supported Molybdenum Oxide Catalysts during Sulfidation," *J. Phys. Chem*, vol. 98, pp. 7862–7870, 1994.

[121] K. S. Liang, J. P. DeNaufville, A. J. Jacobson, R. R. Chianelli, and F. Betts, "Structure of amorphous transition metal sulfides," *J. Non. Cryst. Solids*, vol. 35–36, pp. 1249–1254, Jan. 1980.